Research Square

Preprints are preliminary reports that have not undergone peer review.
They should not be considered conclusive, used to inform clinical practice,
or referenced by the media as validated information.

Hierarchical Porous 2D α-Al2O3 Nanosheet Catalyst for Aminolytic Upcycling of PET Plastic Waste

Putla Sudarsanam

sudarsanam.putla@chy.iith.ac.in

Indian Institute of Technology Hyderabad https://orcid.org/0000-0001-5574-2819

Mudavath Arun Kumar

Indian Institute of Technology Hyderabad

Swapna Bhattu

IIT Hyderabad

Nittan Singh

IIT Hyderabad

Giridhar Madras

IIT Hyderabad

Article

Keywords:

Posted Date: November 14th, 2025

DOI: https://doi.org/10.21203/rs.3.rs-7956009/v1

License: This work is licensed under a Creative Commons Attribution 4.0 International License.
Read Full License

Additional Declarations: There is no conflict of interest

Version of Record: A version of this preprint was published at NPG Asia Materials on July 10th, 2026.
See the published version at https://doi.org/10.1038/s41427-026-00666-3.

Hierarchical Porous 2D α-Al_2O_3 Nanosheet Catalyst for Aminolytic Upcycling of PET Plastic Waste

Mudavath Arun Kumar[a], Bhattu Swapna[a], Nittan Singh[a], Giridhar Madras[b], Putla Sudarsanam*[, a]

[a]Department of Chemistry, Indian Institute of Technology Hyderabad, Kandi 502284, Telangana, India

[b]Department of Chemical Engineering, Indian Institute of Technology Hyderabad, Kandi 502284, Telangana, India

***Email: sudarsanam.putla@chy.iith.ac.in**

Abstract

Despite its wide applicability, the synthesis of α-Al_2O_3 with nanoscale dimensions and a well-developed porous structure continues to be a formidable challenge. This study reports the synthesis of a versatile 2-dimensional α-Al_2O_3 nanomaterial using a simple solution combustion method. The 2D α-Al_2O_3 nanomaterial calcined at 550 °C (denoted as α-Al_2O_3 550) exhibited unique characteristics, including a hierarchical porous structure (5-30 nm), nanosheet morphology (length: 2810-4970 nm, width: 780-973 nm, and thickness: 4.7-9.8 nm), surface-engineered grain boundaries, BET surface area of 56 m^2/g, and optimum amount of acid sites, as confirmed by SEM, TEM, AFM, and NH_3-TPD analyses. The 2D α-Al_2O_3 550 nanosheet catalyst showed excellent activity in upcycling post-consumer PET plastic bottles into a valuable monomer, bis(amino-ethyl) terephthalamide (BAET), using ethylenediamine as both the reactant and solvent. An impressive 92% isolated yield of BAET was achieved over the 2D α-Al_2O_3 550 nanosheet catalyst, outperforming several metal oxides, such as γ-Al_2O_3, Nb_2O_5, CeO_2, and MnO_x. The analysis of the spent α-Al_2O_3 550 catalyst by powder XRD, XPS, and SEM/TEM techniques confirmed its structural and morphological stability. The catalytic process is scalable (5 g), efficiently applied for upcycling different types of post-consumer PET bottles with yields of 80%, and the green chemistry metrics demonstrate the process's sustainability. This study highlights 2D α-Al_2O_3 550 nanomaterial as a robust and economically viable catalyst, offering a practical route for the plastic waste upcycling industry.

Keywords: α-Al_2O_3 nanosheets; Hierarchical porosity; Grain boundaries; Abundant acid sites; Plastic waste upcycling; Value-added monomer

1. Introduction

The diverse properties and extensive applications of plastics from packaging and healthcare to electronics have led to an exponential increase in production to meet the growing global demand [1–5]. However, this increasing reliance on plastics comes at a significant environmental cost, particularly in terms of waste generation and greenhouse gas (GHG) emissions. In 2020, plastic production, processing, and waste management accounted for an estimated 2.45 gigatonnes of CO_2-equivalent (CO_2e) emissions, with about 5% of global industrial GHG emissions [6]. By 2050, this figure is projected to rise to approximately 3.35 gigatonnes CO_2e. The world has produced more than 9.2 gigatonnes of plastic to date. Of this total, nearly 6.9 gigatonnes have never been recycled and instead accumulate in landfills or leak into natural ecosystems. Such inefficiency reflects both a lost economic value and a considerable burden on environmental sustainability[7]. Amid these alarming statistics, recycling emerges as a crucial strategy in mitigating the environmental footprint of plastics. Globally, recycling plastic waste could conserve up to 3.5 billion barrels of oil each year, worth $176 billionconserving valuable resources and reducing dependency on fossil fuels [8]. Moreover, recycling one metric ton of plastic can conserve up to 810 cubic feet of landfill space, conserve 2,600 liters of oil, and reduce energy consumption by nearly 98 million British Thermal Units (BTU).

One of the most widely used plastics, poly(ethylene terephthalate) (PET), makes up almost 12% of all plastic waste [9–11]. Unlike physical methods that rely on a purely mechanical approach, chemical recycling offers a more robust and versatile solution for processing PET waste into high-quality, valuable monomers and chemicals [12]. Various chemical recycling methods were reported for PET waste valorization, such as methanolysis,[13–15] hydrolysis,[16–18] glycolysis,[19–21] and aminolysis [22–26]. PET aminolysis using amine reagents is highly efficient because of the strong nucleophilic nature of the amine nitrogen, which readily reacts with the ester groups of the PET polymer, facilitating the cleavage towards the amide monomers [22–27]. Different types of amine reagents are used, such as ethanolamine,[22] hydrazine monohydride,[28] and diamines [26] for PET aminolysis. Using diamine for PET aminolysis can provide a functional amide monomer with terminal amine groups. Because of these nucleophilic amine groups, the resulting monomer can be used for the synthesis of high-performance polymeric materials, such as polyimines and polyesteramides featuring both imine and amide functionalities[29]. Particularly, the aminolysis of PET using bio-based ethylenediamine (EDA)[30] provides a highly valuable bis(2-aminoethyl) terephthalamide (BAET) monomer. Besides its application in polymer synthesis, BAET can be used for the synthesis of antimicrobial [31,32] and antifungal activity chemicals,[33] as well as in the synthesis of functional perovskite materials [34]. Only a few studies have been reported for PET recycling using diamines to produce BAET and related terephthalamide products. For instance, Honarkar et al. reported PET aminolysis using hydrazine as the diamine source using a homogeneous base catalyst (sodium acetate, NaOAc), achieving an 84.5% yield of terephthalic dihydrazide at 110 °C for 4 h (**entry 1, Figure 1**)[23]. However, the homogeneous nature of NaOAc limits catalyst separation and reusability, while simultaneously deteriorating the quality of the

monomer. Gao and coworkers investigated the reaction of PET with tetramethylenediamine using a phosphonium methyl carbonate-based ionic liquid ([P_{8881}][$MeOCO_2$]) catalyst (**entry 2, Figure 1**)[24]. The catalyst gave 86% yield of monomer at 160 °C for 1 h. Similarly, TBD catalyst was used for the PET aminolysis with ethylenediamine (EDA), affording 89% yield of BAET at 110 °C for 1 h (**entry 3, Figure 1**)[26]. The practical application of organocatalysts is often constrained by complex synthesis routes, catalyst recovery challenges, and energy- or solvent-intensive purification steps. Moreover, organocatalysts are thermally sensitive and prone to degradation during the reaction. These limitations underscore the urgent need for a robust heterogeneous catalyst that can efficiently drive PET aminolysis with EDA under mild conditions, while ensuring thermal stability, cost-effectiveness, and environmental safety.

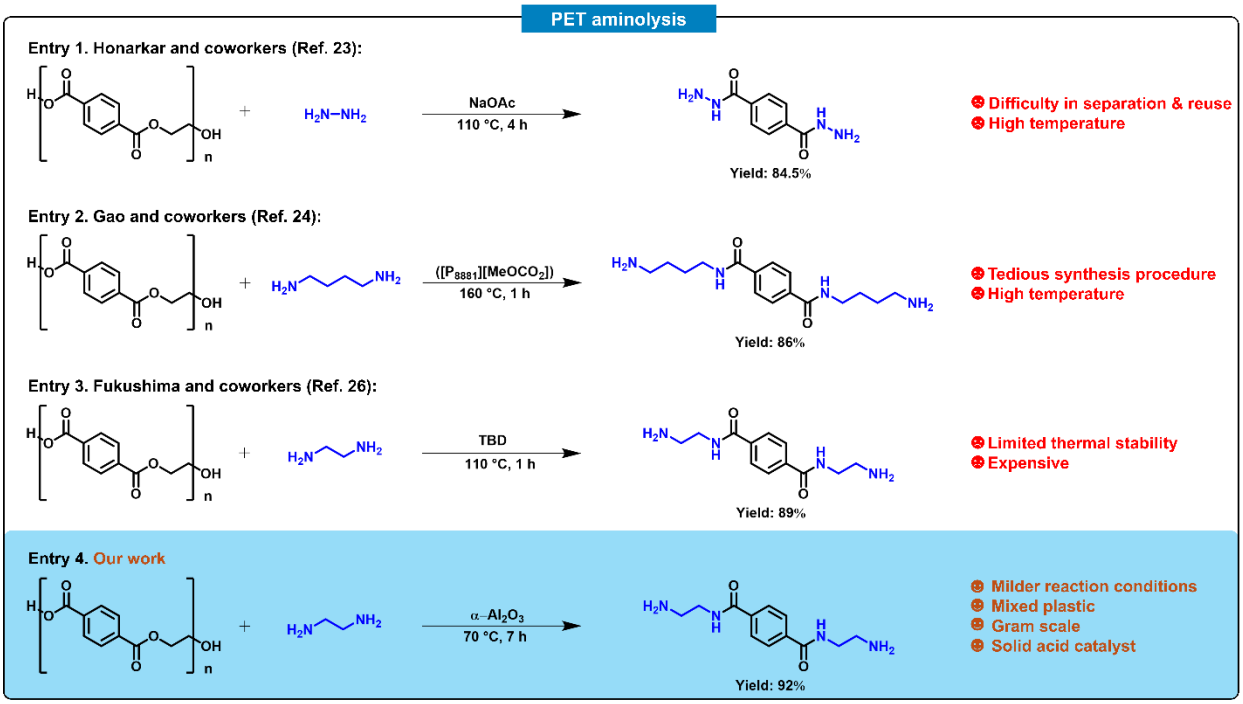


Figure 1. Literature comparison (entries 1-3) for the PET aminolysis with diamines with that of the present work (entry 4). TBD: 1,5,7 triazabicyclo[4.4.0]dec-5-ene.

To develop a cost-effective solution for catalytic plastic waste recycling, Al_2O_3 (corundum) stands out as a practical choice because of its inexpensive and wide availability, with the tunable nature of mild acid-base properties[35–37]. Al_2O_3 exists in several crystalline phases (γ-Al_2O_3, δ-Al_2O_3, θ-Al_2O_3, α-Al_2O_3), of which α-Al_2O_3 is the most thermodynamically and mechanically stable material [38,39]. α-Al_2O_3 phase features a dense trigonal lattice, where O^{2-} ions are placed in a hcp structure with Al^{3+} ions occupying two-thirds of the octahedral sites. This atomic arrangement provides exceptional mechanical strength, thermal stability, and chemical inertness. The synthesis of α-Al_2O_3 is typically achievable only above 1000 °C [40,41]. In this study, a versatile α-Al_2O_3 nanomaterial with distinct characteristics, including a hierarchical porous structure, nanosheet-like morphology, and abundant acid sites, was synthesized at a significantly lower temperature

(500 °C) using a facile solution combustion method [42]. The optimized α-Al_2O_3 catalyst exhibited excellent activity in PET aminolysis with EDA, affording 92% isolated yield of BAET (**entry 4, Figure 1**).

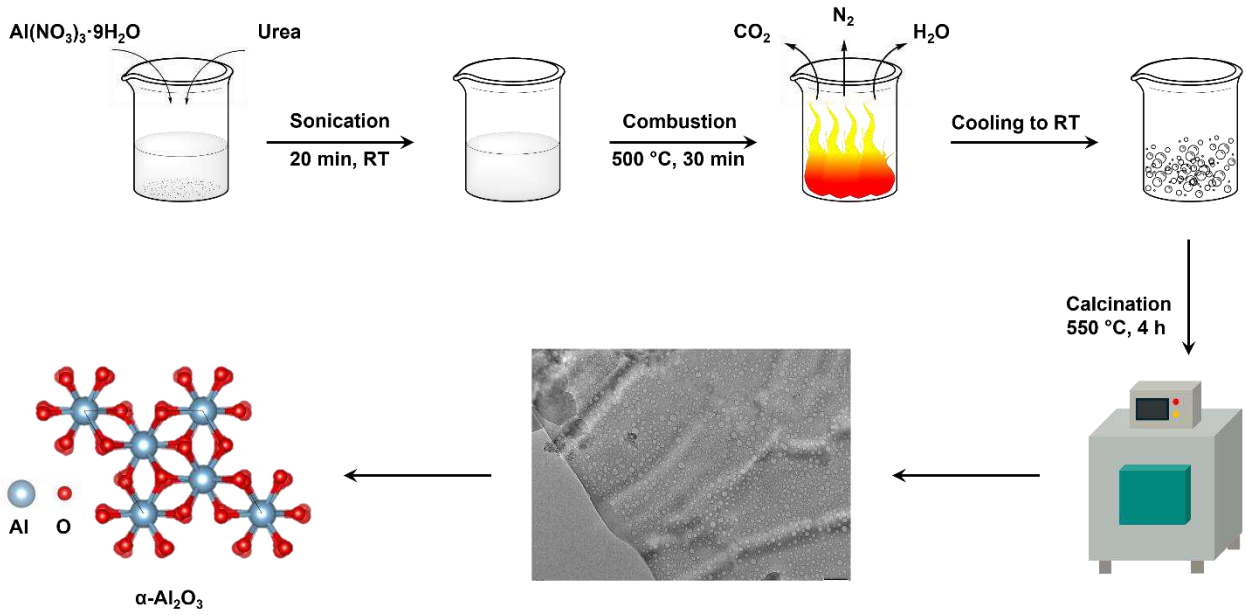


Figure 2. Synthesis procedure of hierarchical porous 2D α-Al_2O_3 nanosheet catalyst using the solution combustion method.

2. Experimental Section

2.1 Catalyst synthesis

The α-Al_2O_3 catalyst was synthesized via the solution combustion synthesis (SCS) method (**Figure 2**). The $Al(NO_3)_3 \cdot 9H_2O$ (Sigma-Aldrich, 99% purity) and the fuel $CO(NH_2)_2$ (SRL, 99% purity) were dissolved in deionized water, sonicated for 20 min, and stirred for another 30 min to obtain a clear solution. The solution was then placed in a muffle furnace pre-heated at 500 °C and maintained at that temperature for 30 min. The resulting white powder was ground and subsequently calcined at 500, 550, and 600 °C for 4 h to obtain the catalysts, labeled as α-Al_2O_3 500, α-Al_2O_3 550, and α-Al_2O_3 600, respectively.

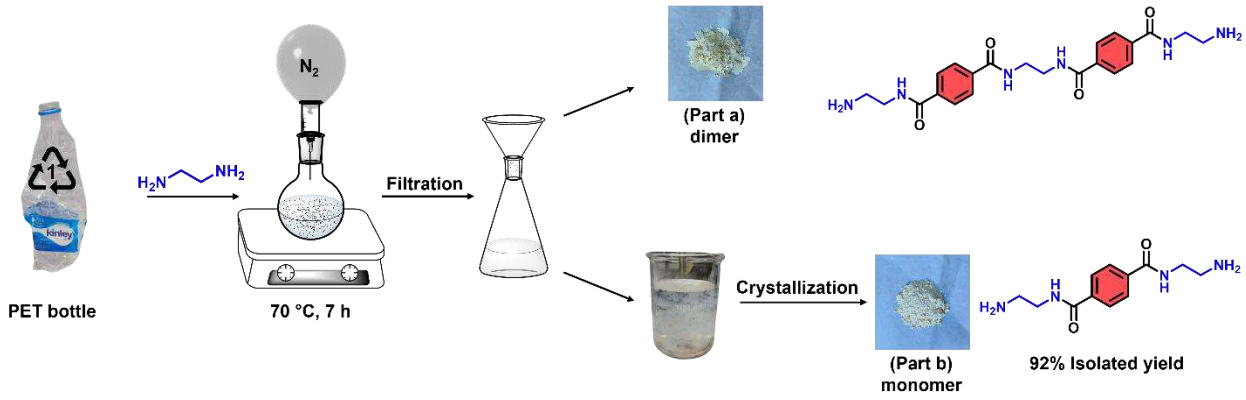
2.2 Catalyst characterization

The details of the analytical techniques used to characterize the catalysts, as well as the PET upcycling products, were provided in the Supporting Information file.

2.3 Reaction procedure of PET aminolysis

A reaction mixture containing 1.0 g (5.2 mmol) of PET bottle chips, 5.5 mL (78 mmol) of

ethylenediamine (EDA), and 50 mg of catalyst was taken in a 50 mL round-bottom flask and heated at 70 °C for 7 h under a nitrogen atmosphere (**Scheme 1**). After the reaction, 10 mL of methanol was added, and the reaction mixture was refluxed for 3 h to solubilize the bis(2-aminoethyl) terephthalamide (BAET) monomer. The setup was then cooled to room temperature and filtered using a methanol–acetone mixture. The insoluble fraction, consisting of depolymerized dimer (**Part a, Scheme 1**), was collected and dried overnight at 80 °C in a vacuum oven. The filtrate contains methanol-soluble BAET monomer, which was gently heated to 50 °C for 15 min to ensure complete dissolution and supersaturation, followed by slow cooling to induce crystallization (**Part b, Scheme 1**). The obtained BAET monomer was collected, washed with methanol and acetone, dried under vacuum at 80 °C overnight, and weighed. The identity and properties of the BAET monomer were confirmed by HR-MS, DSC, TGA, FT-IR, and NMR techniques.



Scheme 1: Reaction procedure for PET aminolysis with ethylenediamine as the amine source.

The PET conversion and the yields of BAET were calculated using the following equations:

$$\text{PET conversion}(\%) = \frac{M_{PET,initial} - M_{PET,residual}}{M_{PET,initial}} \times 100 \qquad \text{eq. 1}$$

where $M_{PET,\ Initial}$, (initial mass), and $M_{PET,\ residual}$ (PET flakes remaining unreacted in the reaction mixture)

$$\text{BAET yield}\ (\%) = \frac{\text{Experimental yield}}{\text{Therotical yield}} \times 100 \qquad \text{eq. 2}$$

3. Results and discussion

3.1 Powder XRD and Raman spectroscopy analyses

The powder XRD analysis showed that the prepared catalysts exhibit distinct and intense diffraction peaks, indicating the highly crystalline nature of α-Al_2O_3 (**Figure 3a**). The peaks appeared at 2θ values of 22.5° (012), 35.2° (104), 37.8° (110), 43.4° (113), 52.6° (024), 57.6°

(116), 61.4° (018), 66.6° (214), and 68.3° (300) belong to the rhombohedral phase of α-Al_2O_3 (corundum, *R3c* space group) [43–45]. The powder XRD pattern of the spent α-Al_2O_3 550 catalyst (**Figure 3a**) showed no significant changes in peak position or intensity compared to the fresh catalyst, confirming the intact structure of the α-Al_2O_3 catalyst during the reaction. For comparison, the XRD pattern of γ-Al_2O_3 550 (cubic phase) was also provided (**Figure 3a**). Various Raman bands at 373, 413, 452, 570, 640, and 743 cm^{-1}, corresponding to E_g, A_{1g}, E_g, E_g, A_{1g}, and E_g vibrational modes, were noticed in all the samples (**Figure 3b**) [46,47]. A minor peak at 373 cm^{-1} and a broad peak at 452 cm^{-1} belong to bridged Al–O–Al vibrational modes [42,48,49]. The minor peaks at 413, 570, 640, and 743 cm^{-1} belong to Al–O vibrational modes [39,50,51].

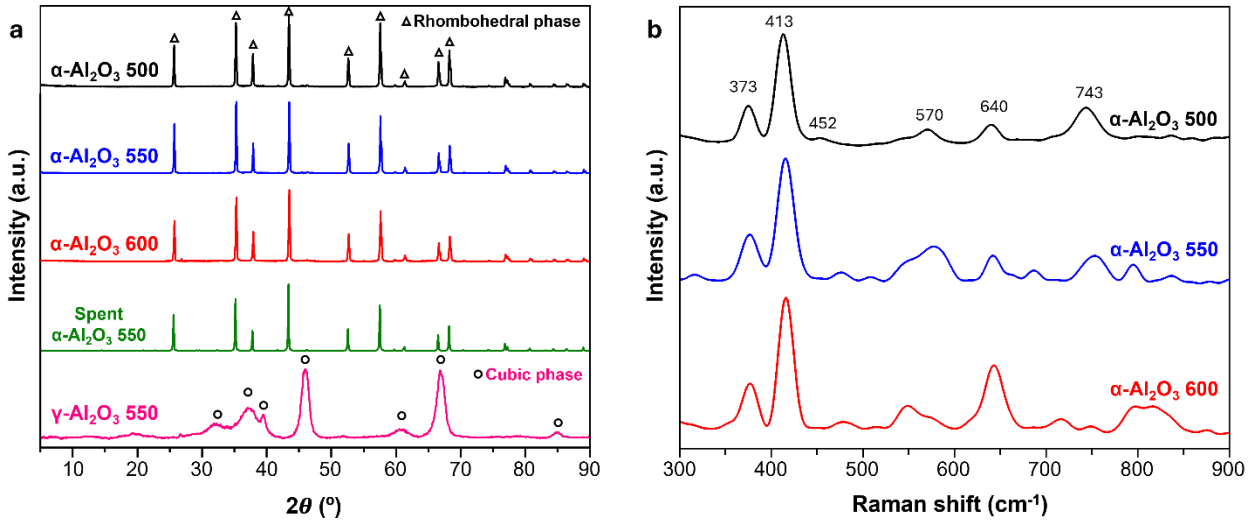


Figure 3. (a) Powder XRD profiles and (b) Raman spectra of α-Al_2O_3 catalysts.

3.2 TEM, SEM, and AFM analyses

The morphology and nanostructure of the α-Al_2O_3 catalysts studied by microscopic techniques. TEM images show the presence of sheet-like particles (length: 2810-4970 nm) with small pit-like pores (5-30 nm) distributed throughout the surface in all the α-Al_2O_3 catalysts (**Figure 4**) [38,42,52]. In solution combustion synthesis (**Figure 2**), urea is taken as a fuel that undergoes thermal decomposition and combustion, releasing various gases (NHCO, NH_3, N_2O_4, NO_2, and N_2O_5) by facilitating pores within the catalyst structure [53–56]. These nanosheets with a unique arrangement of pores can be highly beneficial for heterogeneous catalytic applications while providing enhanced mass transport properties and controlled reaction mechanisms. The HR-TEM images confirm the crystalline nature of the α-Al_2O_3 550 material, with fringes oriented along different directions corresponding to specific planes (**Figure S1, Supporting Information**). The measured d-spacing value of 0.208 nm for the (113) plane of α-Al_2O_3 550 is consistent with powder XRD analysis [57]. After the reaction, the α-Al_2O_3 550 catalyst retains its original morphology, resembling its great stability during the reaction (**Figure 4d**).

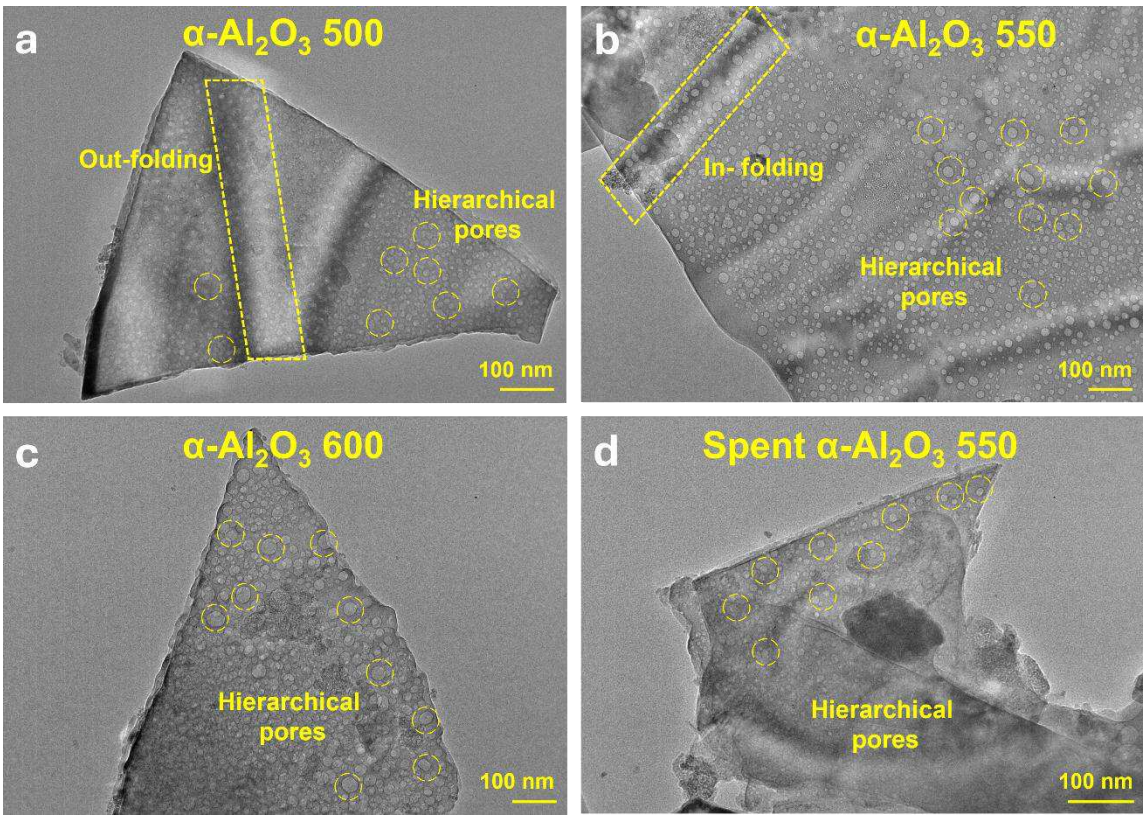


Figure 4. TEM images of (a) α-Al_2O_3 500, (b) α-Al_2O_3 550, (c) α-Al_2O_3 600, and (d) spent α-Al_2O_3 550 catalysts.

The SEM images of α-Al_2O_3 550 captured along different orientations reveal a sheet-like morphology (**Figure 5**), which is consistent with the TEM observations (**Figure 4**). The presence of surface and edge pores in the α-Al_2O_3 550 sheets highlights the versatile nature of the material, making it suitable for a wide range of energy and environmental applications **(Figure 5c,d)**. In addition, the α-Al_2O_3 550 sheets exhibit well-defined grain boundaries throughout the sample, which can provide abundant active sites and simultaneously facilitate enhanced mass diffusion for catalytic applications (**Figure 5a,b).** AFM analysis provided further insights into the morphology of the α-Al_2O_3 550 nanosheets (**Figure 6**)[38,58,59]. The two-dimensional AFM image **(Figure 6a)** clearly reveals the nanosheet morphology, and the corresponding height profile **(Figure 6b)** shows an average thickness ranging from approximately 4.7 to 9.8 nm. The TEM image **(Figure 6c)** displays distinct surface foldings along with uniformly distributed pores. Similarly, the three-dimensional AFM image **(Figure 6d)** highlights comparable folding features, corroborating the TEM results and confirming that the majority of the α-Al_2O_3 nanosheets adopt this folded morphology.

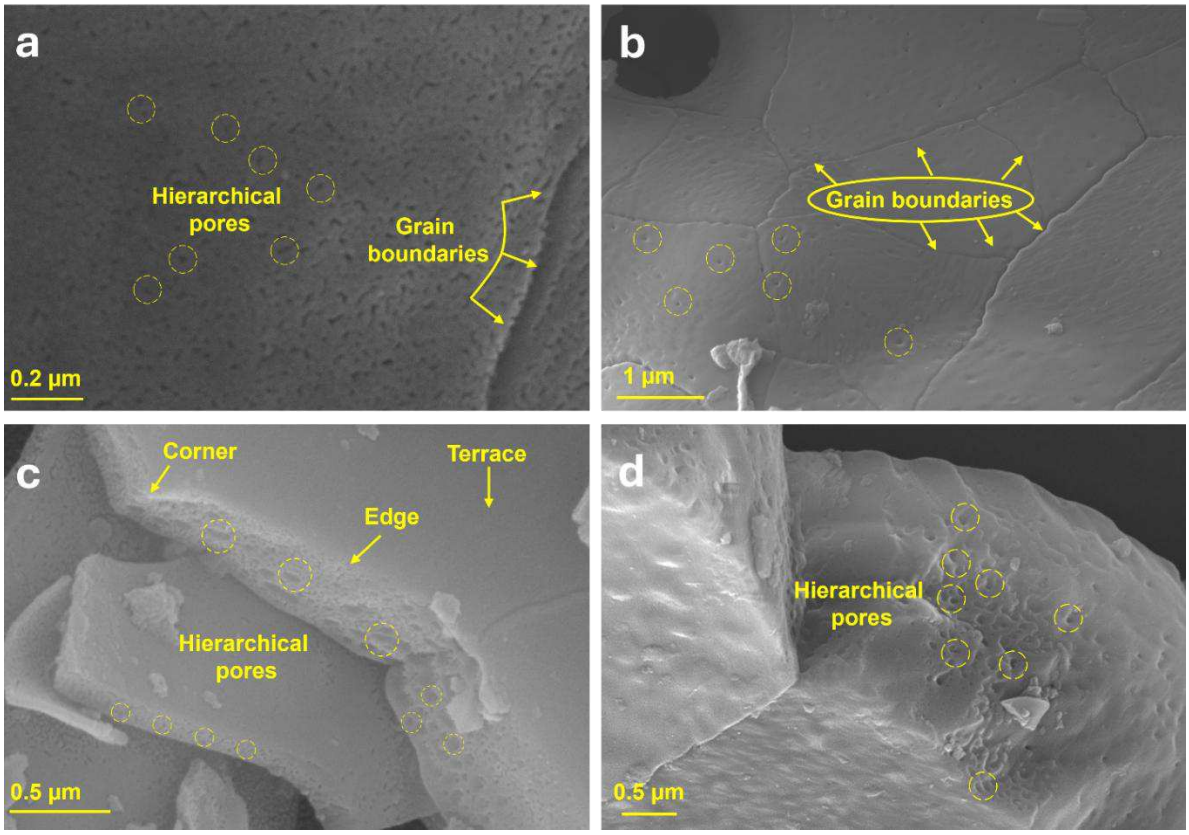


Figure 5. SEM images of α-Al_2O_3 550 highlighting (a) porous surface, (b) grain boundaries, and (c-d) pores on the edges and corners.

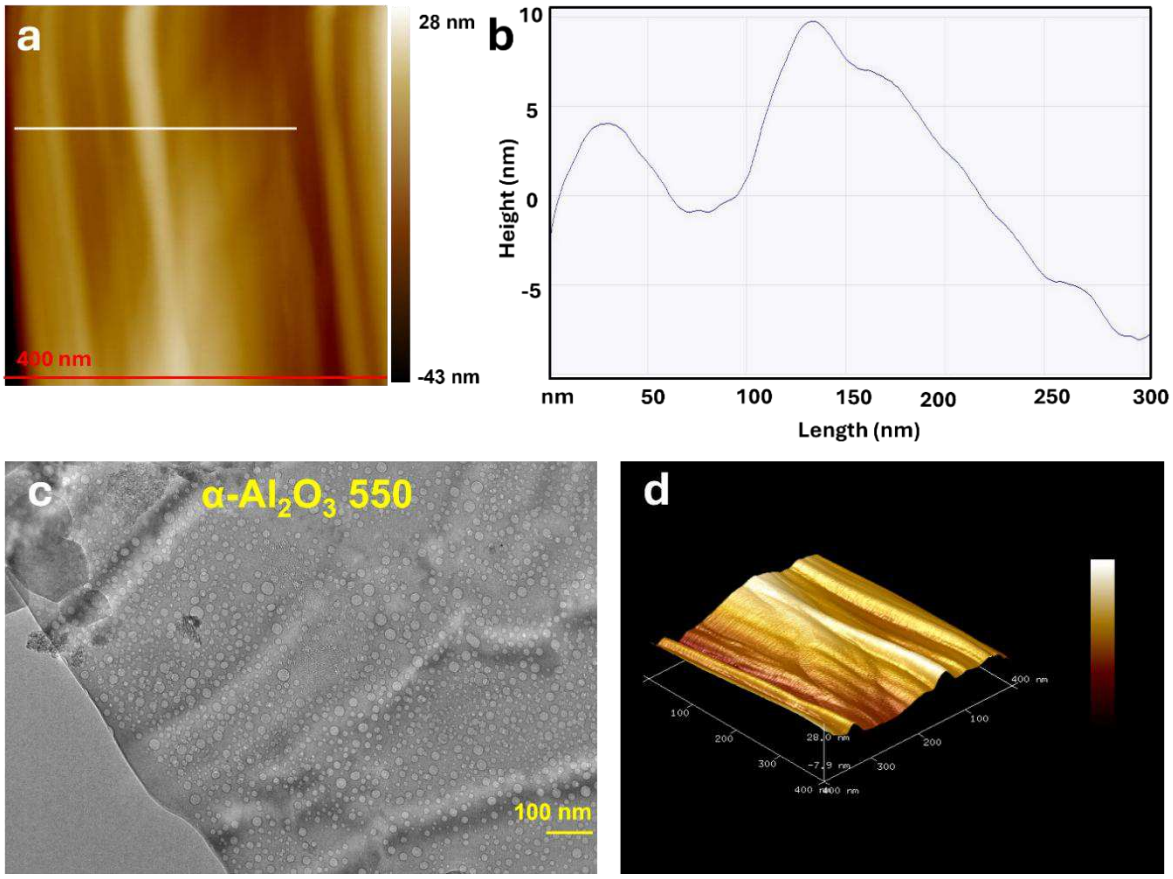


Figure 6. (a) Two-dimensional AFM image of α-Al_2O_3 550 nanosheets, (b) height profile of the white line in the AFM image, (c) TEM image of α-Al_2O_3 550 nanosheets, and (d) three-dimensional topographic AFM image of α-Al_2O_3 550 nanosheets.

3.3 N_2 adsorption-desorption, XPS, and NH_3-TPD analyses

All Al_2O_3 catalysts showed type IV isotherms with an H3 hysteresis loop, indicating open pores (**Figure 7a**), which are clearly visible in TEM (**Figure 4**) and SEM (**Figure 5**) images [44,57,60–62]. The BET surface area of the samples (**Table 1**) follows: α-Al_2O_3 550 (56 m^2/g) > α-Al_2O_3 500 (30 m^2/g) > α-Al_2O_3 600 (24 m^2/g). The low BET surface area of α-Al_2O_3 600 is due to particle aggregation at the elevated calcination temperatures (600 °C). The pore volume and pore size of Al_2O_3 catalysts were in the range of 0.022–0.053 cm^3/g and 3.4–3.6 nm, respectively (**Table 1**).

XPS analysis was conducted to investigate Al and O's oxidation states and the impact of calcination temperature on the chemical environment of these species in the Al_2O_3 catalysts (**Figure 7**). All the samples showed an Al 2p XPS peak at 73.8-74.0 eV (Al $2p_{3/2}$), corresponding to Al^{3+} species (**Figure 7b**) [63,64]. The Al 2p XPS peak of α-Al_2O_3 is shifted to lower binding energies with the increase of calcination temperature from calcined at 500 °C to 550 °C and 600 °C, showing a shift towards lower binding energies (**Figure 7b**), indicating the structural perturbations at elevated calcination temperatures [65,66]. The deconvolution of O 1s XP spectra shows two peaks:

(i) lattice oxygen (Al-O) at 530.66–530.81 eV and (ii) surface hydroxy groups (Al-OH) at 532.53–532.57 eV (**Figure 7c**)[67–69]. The Al 2p (**Figure S2a, Supporting Information**) and O 1s (**Figure S2b, Supporting Information**) of spent α-Al_2O_3 550 catalysts closely resemble those of the fresh catalyst, indicating the structural stability of the catalyst during the reaction.

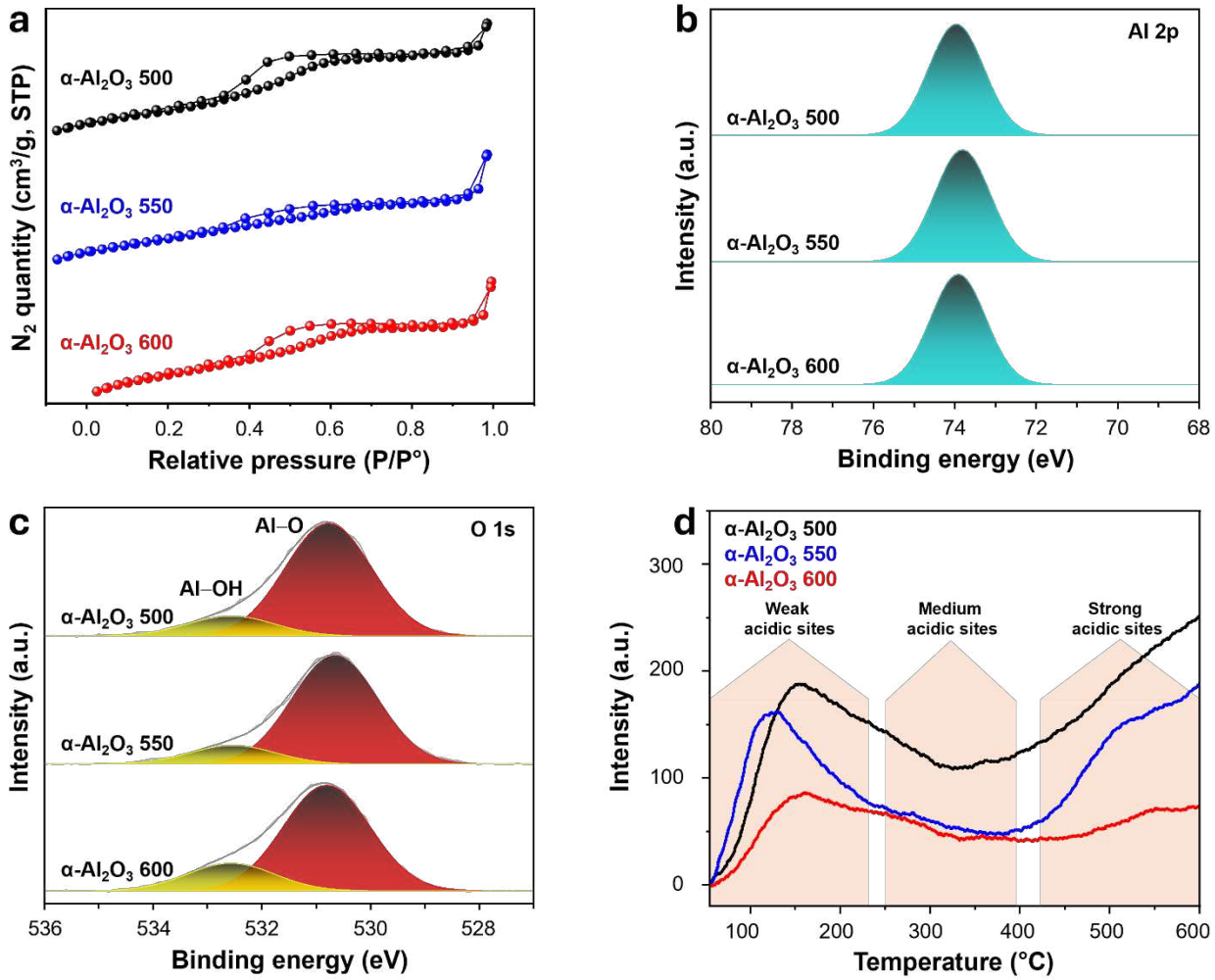


Figure 7. (a) N_2 adsorption-desorption isotherms, (b) Al 2p XP spectra, (c) O 1s XP spectra, and (d) NH_3-TPD profiles of α-Al_2O_3 catalysts.

Since the acid sites of the catalysts play a crucial role in PET aminolysis, NH_3-TPD analysis was conducted to evaluate the surface acidity of the α-Al_2O_3 catalysts (**Figure 7d**). The acidity strength of α-Al_2O_3 catalysts depends on the calcination temperature and the synthesis method. As shown in **Figure 7d,** the NH_3 desorption peak in the range of 50-250 ºC indicates weak acidic sites in all catalysts [70–72]. The α-Al_2O_3 500 and α-Al_2O_3 600 catalysts exhibit only weak acidic sites. In contrast, the α-Al_2O_3 550 catalyst possesses a broad peak at 450-600 ºC, corresponding to strong acidic sites (**Figure 7d**). The strong acidity of the α-Al_2O_3 550 catalyst arises from the low-coordinated and electron-deficient Al^{3+} sites. These sites are found at the well-defined grain boundaries and within the pores on the surface edges and corners of the nanosheets (**Figure 5**)

[62,70,73]. The superior activity of the α-Al_2O_3 550 catalyst in PET aminolysis can be attributed to strong acidic sites [61,74].

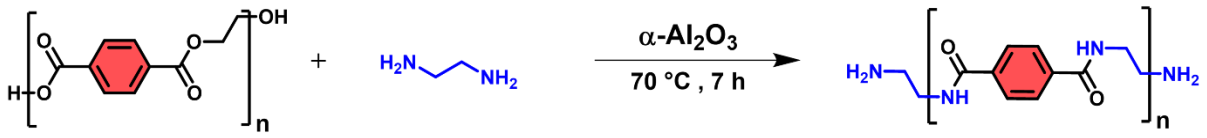
Table 1: BET surface area, average pore volume, and average pore size of α-Al_2O_3 catalysts.

Entry	Catalyst	BET surface area (m^2/g)	Average pore volume (cm^3/g)	Average pore width (nm)
1	α-Al_2O_3 500	30	0.026	3.46
2	α-Al_2O_3 550	56	0.053	3.53
3	α-Al_2O_3 600	24	0.022	3.62

3.4 Catalyst screening for PET aminolysis

PET aminolysis was conducted using ethylenediamine (EDA) as the amine source at 70 °C for 7 h and a 1:15 molar ratio of PET:EDA (1 g PET). The aminolysis reaction was initially performed using α-Al_2O_3 catalysts calcined at different temperatures. Among them, the α-Al_2O_3 catalyst calcined at 550 °C (α-Al_2O_3 550) exhibited the highest BAET yield of 92% **(entry 2, Table 2)**. α-Al_2O_3 catalysts calcined at 500 °C and 600 °C yielded 80% **(entry 1, Table 2)** and 75% **(entry 3, Table 2)** BAET, respectively. The γ-Al_2O_3 catalyst calcined at 550 °C **(entry 4, Table 2)** achieved a lower yield of 76%, underscoring the higher activity of the α-Al_2O_3 550 catalyst (**entry 2, Table 2**). Nb_2O_5 catalyst **(entry 5, Table 2)**, previously reported by our group for PET aminolysis,[25] gave a 78% BAET yield. Commercial metal oxides showed significantly lower activity: 25% **(entry 6, Table 2)**, 16% **(entry 7, Table 2)**, 20% **(entry 8, Table 2)**, and 13% **(entry 9, Table 2)** BAET yields over α-Al_2O_3, Nb_2O_5, Mn_2O_3, and CeO_2, respectively. These results highlight the superior catalytic performance of the synthesized α-Al_2O_3 550 catalyst for PET upcycling via aminolysis to achieve higher yields of BAET monomer.

Table 2. Catalyst screening for PET aminolysis with ethylenediamine (EDA)[a]



Entry	Catalyst	BAET yield[h] (%)
1	α-Al_2O_3 500	80
2	α-Al_2O_3 550	92
3	α-Al_2O_3 600	75
4[b]	γ-Al_2O_3 550	76

Entry	Catalyst	BAET yield[h] (%)
5	Nb_2O_5	78
6[c]	Commercial α-Al_2O_3	25
7[d]	Commercial Nb_2O_5	16
8[e]	Commercial Mn_2O_3	20
9[f]	Commercial CeO_2	13
10[g]	α-Al_2O_3 550	90

[a]**Reaction conditions**: 5 wt% catalyst (50 mg) with respect to PET (1 g), 70 °C reaction temperature, 7 h reaction time, and 1:15 molar ratio of PET to EDA. [b] γ-Al_2O_3 550 catalyst. [c]α-Al_2O_3 (SRL, 99.9% purity). [d]Nb_2O_5 (SRL, 99.9% purity). [e]Mn_2O_3 (SRL, 99.9% purity). [f]CeO_2 (SRL, 99.9% purity). [g]Large-scale: 5 g PET, 25 ml EDA, 250 mg α-Al_2O_3 550 catalyst, 70 °C reaction temperature, and 10 h reaction time. [h]Error (isolated BAET yield): ±3%.

3.5 Characterization of reaction products (BAET monomer and dimer)

PET aminolysis with ethylene diamine gives two major products, namely bis(2-aminoethyl) terephthalamide (BAET monomer) and a dimer (**Scheme 2a)**. The reaction between PET and EDA gives amide (**i, Scheme 2b**) and ester oligomers (**ii, Scheme 2b**). The subsequent reaction of amide oligomers with the excess amount of EDA gives the BAET monomer. Simultaneously, the coupling of amide-based oligomers (**i in Scheme 2b, Figures S18, S21, S24, Supporting Information**) and ester-based oligomers (**ii in Scheme 2b, Figures S19, S20, S22, Supporting Information**), to form the intermediate structure (**iii in Scheme 2b**, **Figures S27-S30, Supporting Information**), followed by the attack of EDA gives the dimer (**Figure S9**, **Supporting Information**), trimer (**Figure S16**, **Supporting Information**), and tetramer (**Figure S17**, **Supporting Information**). The procedure for the separation of BAET and AOET (dimer) was provided in Section 2.3 (**Scheme 1**)[75,76]. Both BAET monomer and AOET dimer were characterized by various techniques, such as NMR, FT-IR, HR-MS, TGA, and DSC. The FT-IR spectrum of PET (**Figure S3, Supporting Information**) displayed characteristic absorption bands at 1502 and 1579 cm^{-1} (aromatic C=C), 2958 cm^{-1} (–CH_2–), 3440 cm^{-1} (–OH), 1710 cm^{-1} (ester C=O), and 1412 cm^{-1} (C–O deformation), confirming its typical polyester structure[77,78]. Upon aminolysis, the disappearance of the ester C=O band at 1710 cm^{-1}, along with the emergence of a new amide C=O band at 1629 cm^{-1} confirmed the formation of BAET and AOET (dimer) dimer (**Figure S3, Supporting Information**). Both products also exhibited prominent N–H stretching bands, corresponding to primary (3341 cm^{-1}) and secondary (3281 cm^{-1}) amines, with BAET showing higher intensity due to its terminal -NH_2 groups. Additionally, symmetric and asymmetric

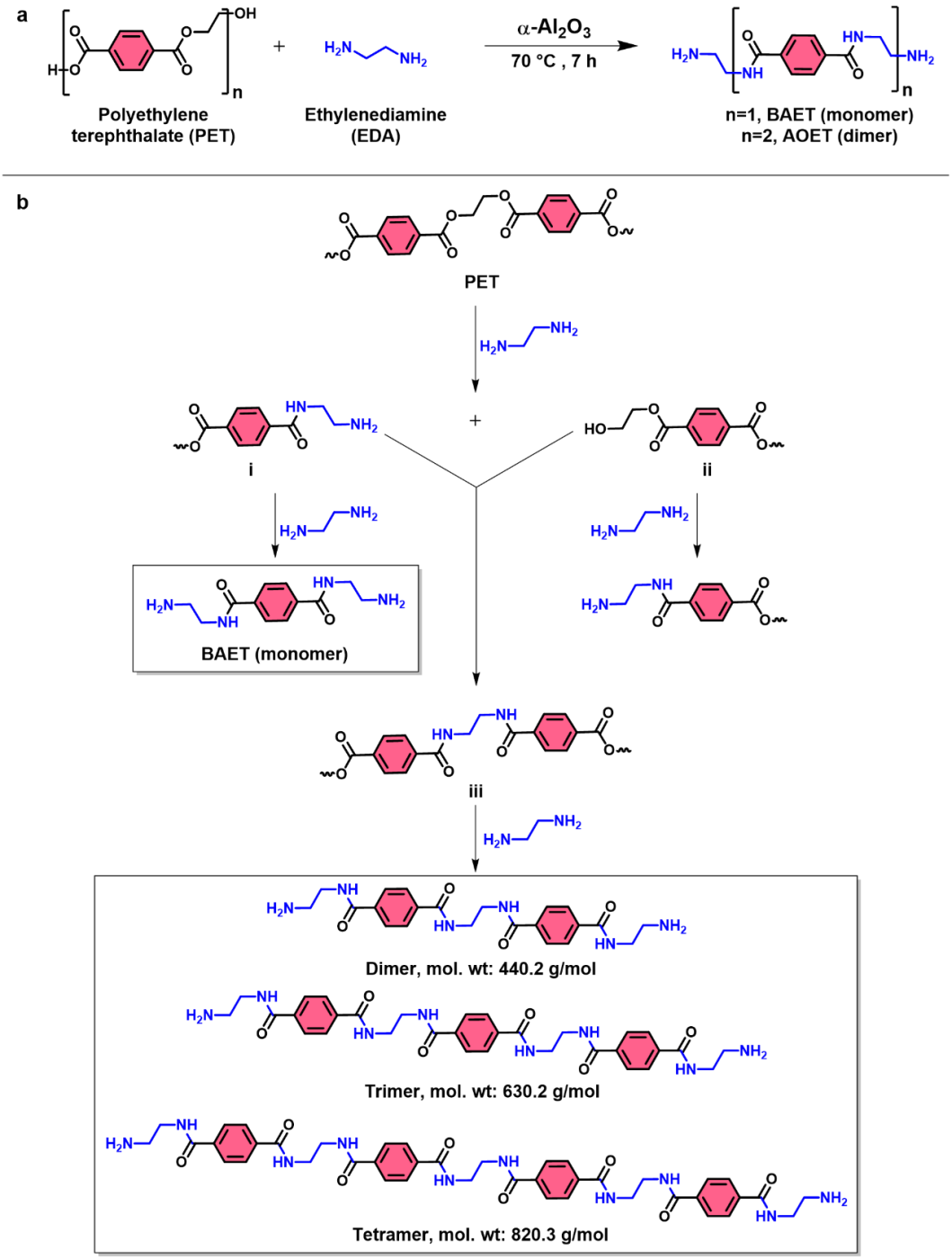
–CH_2– vibrations at 2950 and 2872 cm^{-1}, along with a distinct para-substituted aromatic C–H bending vibration at 860 cm^{-1}, were observed in all three structures (PET, BAET, and AOET).

The NMR analysis confirmed the structure and purity of BAET and AOET (dimer) dimer products. The ^{1}H NMR spectrum (acetic acid-d_4) of BAET showed peaks at ~8.0 ppm (s, 4H, Ar-***H***), 3.84 –3.81 ppm (m, 4H, NH***CH₂***), and 3.42–3.39 ppm (m, 4H, ***CH₂***NH_2) (**Figure S4, Supporting Information**)[26,75,76]. The ^{13}C NMR spectrum of BAET monomer shows peaks at δ 169.94 ppm (2C, ***C=O***), 137.23 ppm (2C ***Ar-C***), 128.68 ppm (***Ar C-H***), 40.75 ppm (2C NH***CH₂***), and 38.64 ppm (***CH₂***NH_2) (**Figure S5, Supporting Information**)[76]. The ^{1}H NMR spectrum of AOET (dimer) dimer shows resonances at ~8.0 ppm (8H, s, Ar-***H***), 3.82–3.80 ppm (m, 4H, NH***CH₂***), 3.76 ppm (s, 4H, NH***CH₂CH₂***NH), and 3.40–3.39 ppm (m, 4H, ***CH₂***NH_2) (**Figure S6, Supporting Information**)[75]. A new peak at 3.75 ppm is observed in AOET (dimer) dimer when compared with BAET, which can be attributed to the presence of a symmetrical ethyl group attached to the amide moieties. The ^{13}C NMR spectrum of AOET (dimer) shows peaks at δ 170.01 and 169.80 ppm (4C, ***C=O***), 137.81 and 137.07 ppm (4C, ***Ar-C***), 128.76 and 128.55 ppm (8C, ***Ar C-H***), 40.81 ppm (4C, NH***CH₂***), and 38.67 (2C, ***CH₂***NH_2) ppm (**Figure S7**, **Supporting Information**)[76].

The HR-MS analysis (**Figure S8, Supporting Information**) exhibited a peak at *m/z* 273.1303, corresponding to BAET ionized by Na^+ $[BAET + Na]^+$, and the molecular formula is $C_{12}H_{18}N_4O_2$. The HR-MS peak at *m/z* 441.22 corresponds to the AOET (dimer) ionized by H^+, while another peak at *m/z* 463.20 represents the AOET (dimer) ionized by Na^+ (**Figure S9, Supporting Information**). A peak at *m/z* 479.1812 is also attributed to the AOET (dimer) ionized by K^+ as $[AOET (dimer) + K]^+$. This data further confirmed the formation of the AOET (dimer) with the molecular formula $C_{22}H_{28}N_6O_4$.

DSC and TGA analyses revealed distinct thermal behaviors for PET and its aminolysis products. PET displayed a sharp melting point at ~245 °C and underwent a single-step thermal decomposition starting at ~400 °C (**Figure S10, Supporting Information**)[75]. In contrast, BAET and AOET (dimer) products showed significantly different thermal profiles. The TGA thermogram (**Figure S11a, Supporting Information**) reveals that BAET experienced a 14.6 wt% weight loss between 96–170 °C, followed by a major 62.1 wt% loss between 181–330 °C, and an additional 13.2 wt% loss between 330–586 °C. The differential weight loss curves (**Figure S11b, Supporting Information**) display three prominent peaks, with T_{1max} occurring at 170 °C, T_{2max} at 270 °Cand T_{3max} at 330 °C. The 14.6% weight loss at 170 °C in the TGA curve coincides with the melting point of BAET identified by DSC, indicating that melting is accompanied by partial thermal decomposition[76]. The DSC traces of BAET and AOET (dimer) are presented in **Figure S11b, Supporting Information**. Sharp endothermic peaks at 171 °C and 320 °C belong to the melting points of BAET and AOET (dimer), respectively. These melting points are significantly higher than those of terephthalates obtained via PET glycolysis using ethylene glycol, where bis(hydroxyethyl) terephthalate (BHET) exhibits a melting point below 110 °C [20,75]. This notable

difference in thermal behavior between PET glycolysis and aminolysis products is primarily attributed to the rigid molecular structure of the diamine. The high melting points of BAET and AOET (dimer) are associated with stiff structural elements, terephthalate units, amide bonds, and the strong secondary interactions expected between amide and amine groups[79].



Scheme 2. (a) Aminolysis of PET. (b) Formation of PET aminolysis products: BAET (monomer), dimer, trimer, and tetramer.

3.6 Effect of reaction temperature, ethylenediamine amount, and reaction time

The reaction conditions for PET depolymerization with EDA over the α-Al_2O_3 550 catalyst were systematically optimized to maximize BAET yield. As shown in **Figure 8a**, increasing the temperature steadily improved the BAET yield from 58% at 50 °C to 72% at 60 °C, and reached a maximum yield (92%) at 70 °C. However, further raising the temperature to 80 °C caused a considerable drop in yield to 80%, highlighting the importance of maintaining optimal thermal conditions for efficient depolymerization. Similarly, the effect of EDA concentration was studied as EDA serves both as the amine source and solvent, diffusing into solid PET flakes to swell the polymer and thereby facilitating the depolymerization into the BAET monomer. Therefore, maintaining an optimal PET:EDA molar ratio is essential. As shown in **Figure 8b**, increasing the molar ratio of PET:EDA from 1:5 to 1:10 enhanced PET conversion from 60% to 80% and BAET yield from 73% to 82%, indicating that insufficient EDA limits PET dissolution and depolymerization. At a 1:15 ratio, complete PET conversion and a high BAET yield of 92% were achieved. Increasing the ratio further to 1:20 maintained full PET conversion but reduced BAET yield to 81%, likely due to enhanced rates of parallel reactions. As described in **Scheme 2b**, EDA initially reacts with PET to form an amide-based oligomer ($RCONHCH_2CH_2NH_2$) (**Figures S18, S21, S24**, **Supporting Information**), which can subsequently react with additional ester groups of PET to form dimer (**Figure S9, Supporting Information**), trimer (**Figure S16, Supporting Information**), and tetramer (**Figure S17, Supporting Information**), thus reducing the BAET selectivity[23,75,76].

Reaction time plays a critical role in the PET aminolysis reaction to produce BAET monomer (**Figure 8c**). Using 5 wt% α-Al_2O_3 550 catalyst at 70 °C and a PET:EDA molar ratio of 1:15, both PET conversion and BAET yield were monitored over a reaction period of 1 to 8 h. After 1 h, PET conversion reached 20%, with a corresponding BAET yield of 8%. As the reaction progressed, conversion and yield steadily increased to 48% and 20% at 2 h, 78% and 57% at 4 h, respectively, ultimately reaching full PET conversion and a 92% BAET yield after 7 h. The aminolysis proceeds via an equilibrium-controlled mechanism (**Scheme 4**). Prolonging the reaction to 8 h led to a decrease in BAET yield to 76%, likely due to the backward reaction and/or further conversion into the AOET (dimer).

To evaluate the versatility and broader applicability of the optimized reaction protocol, different real-world colored PET waste bottles were shredded into small pieces and subjected to aminolysis. The study demonstrated that PET bottles of varying colors, including white, green, purple, and a mixture of white, green, and purple, were effectively depolymerized into pure BAET, as summarized in **Table S1 (Supporting Information)**. A gradual decline in BAET yield from 92% (white PET) to 82% (green PET) to 80% (purple PET) was observed, which can be attributed to the increased rigidity of PET as well as the presence of dyes and additives incorporated during manufacturing[80]. Interestingly, mixed PET waste still produced BAET with a high yield of 80%. The consistently good-to-excellent BAET yields from differently colored PET samples highlight

the developed catalyst's robustness and suitability for practical applications. The large-scale experiment (5 g PET waste) provided a 90% yield of BAET monomer (**entry 10, Table 2**).

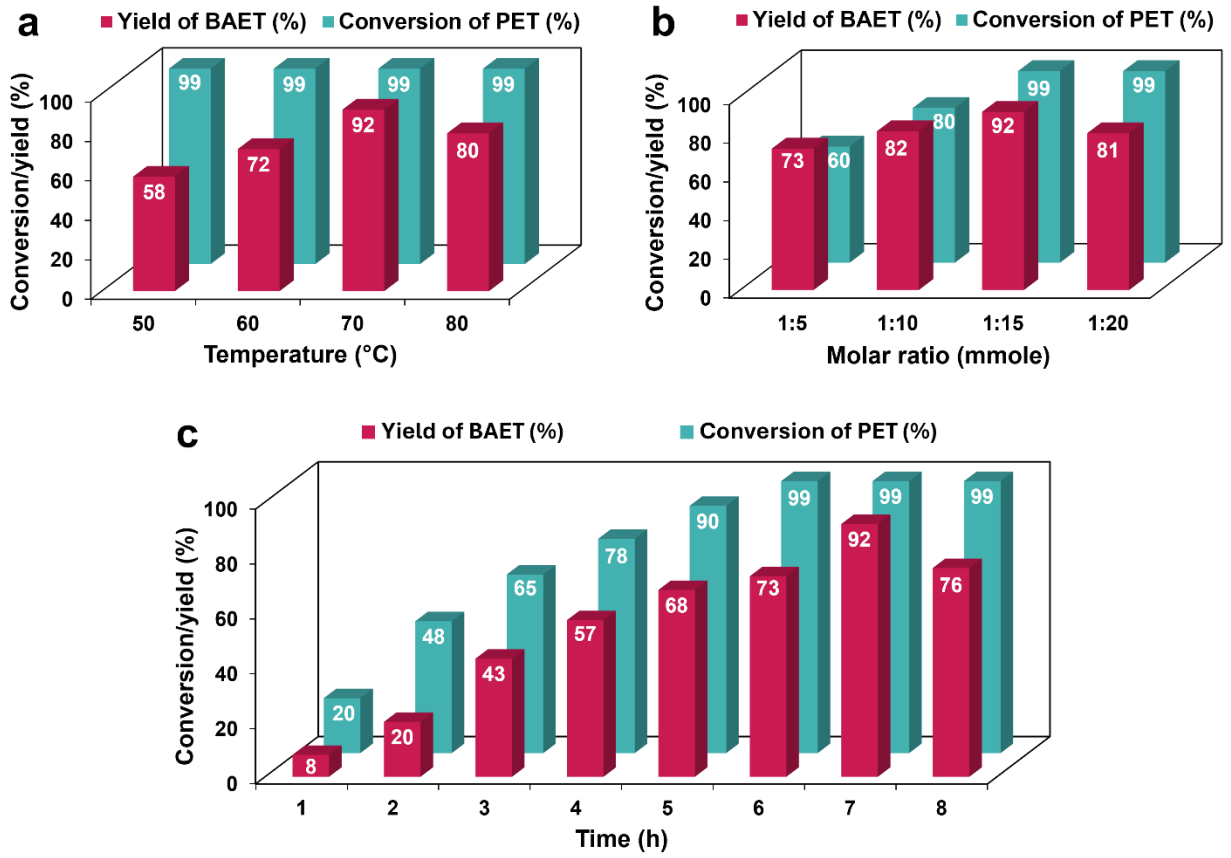


Figure 8. (a) Effect of reaction temperature (reaction conditions: 5 wt% catalyst with respect to PET, 7 h reaction time, and 1:15 molar ratio of PET to EDA), (b) effect of molar ratio of PET:EDA (reaction conditions: 5 wt% catalyst with respect to PET, 70 °C temperature, and 7 h), and (c) effect of reaction time (reaction conditions: 5 wt% catalyst with respect to PET, 70 °C reaction temperature and 1:15 molar ratio of PET to EDA) in the PET aminolysis using the α-Al_2O_3 550 catalyst. Error (isolated BAET yield): ±3%.

3.7 Calculations of green chemistry metrics

The green chemistry metrics were assessed to evaluate the efficiency of raw material and energy use, while also considering waste minimization and the avoidance of hazardous solvents [80]. The complete equations and calculations are provided in **Section S2, Supporting Information**, and the respective results are shown in **Table 3**. The environmental factor (E-factor) quantifies the waste produced during the reaction, where a higher value reflects a greater environmental burden[67]. For the aminolysis of PET, the E-factor was found to be 0.45 (**entry 1, Table 3**), which indicates reduced waste generation compared to conventional processes. The energy economy coefficient

(ε), which relates product yield to reaction time and temperature, was calculated as 3.1×10^{-5} (**entry 2, Table 3**). Higher ε values suggest high energy efficiency and economic viability.

The solvent intensity (SI) measures the amount of solvent consumed in relation to the product mass, where higher values indicate greater solvent use and higher process costs. In the aminolysis of PET, ethylenediamine functions as the reactant itself, eliminating the requirement for any additional solvent, resulting in an SI value of 0 (**entry 3, Table 3**). The process mass intensity (PMI) extends this concept by considering the total mass of all reactants and catalysts relative to the product. PMI values of 5.05 (**entry 4, Table 3**) were obtained, confirming efficient material use and limited environmental impact. To further assess sustainability, renewable intensity (RI) and renewable percentage (RP) were calculated. RI is obtained by comparing the mass of renewable-derived inputs to the product mass, yielding values of 4.18 (**entry 5, Table 3**). RP, calculated by relating RI to PMI, was 82.77% (**entry 6, Table 3**), demonstrating that most inputs were renewable or recyclable. The primary reaction products are BAET, AOET (dimer), and their oligomers. We evaluated the BAET mass formed during purification to calculate the carbon ratio. The solid conversion rate aligns with the carbon ratio of 91.41% before and after the reaction. **S3, Supporting Information**, provides the comprehensive calculation. Collectively, the low E-factor, favorable PMI, and high RP highlight that PET aminolysis to BAET operates with minimal environmental impact and strong alignment with the principles of green chemistry.

Table 3. Green metrics calculations for the PET aminolysis using ethylenediamine as an amine source to yield BAET monomer. Reaction conditions: 50 mg α-Al_2O_3 550 catalyst, 70 °C reaction temperature, 7 h reaction time, and 1:15 molar ratio of PET to EDA.

Entry	Green chemistry parameters	PET aminolysis to BAET values
1	Environmental factor (E-factor)	0.45
2	Energy economy coefficient (ε)	3.1×10^{-5}
3	Solvent intensity (SI)	0
4	Process mass intensity (PMI)	5.05
5	Renewable intensity (RI)	4.18
6	Renewable percentage (RP)	82.77

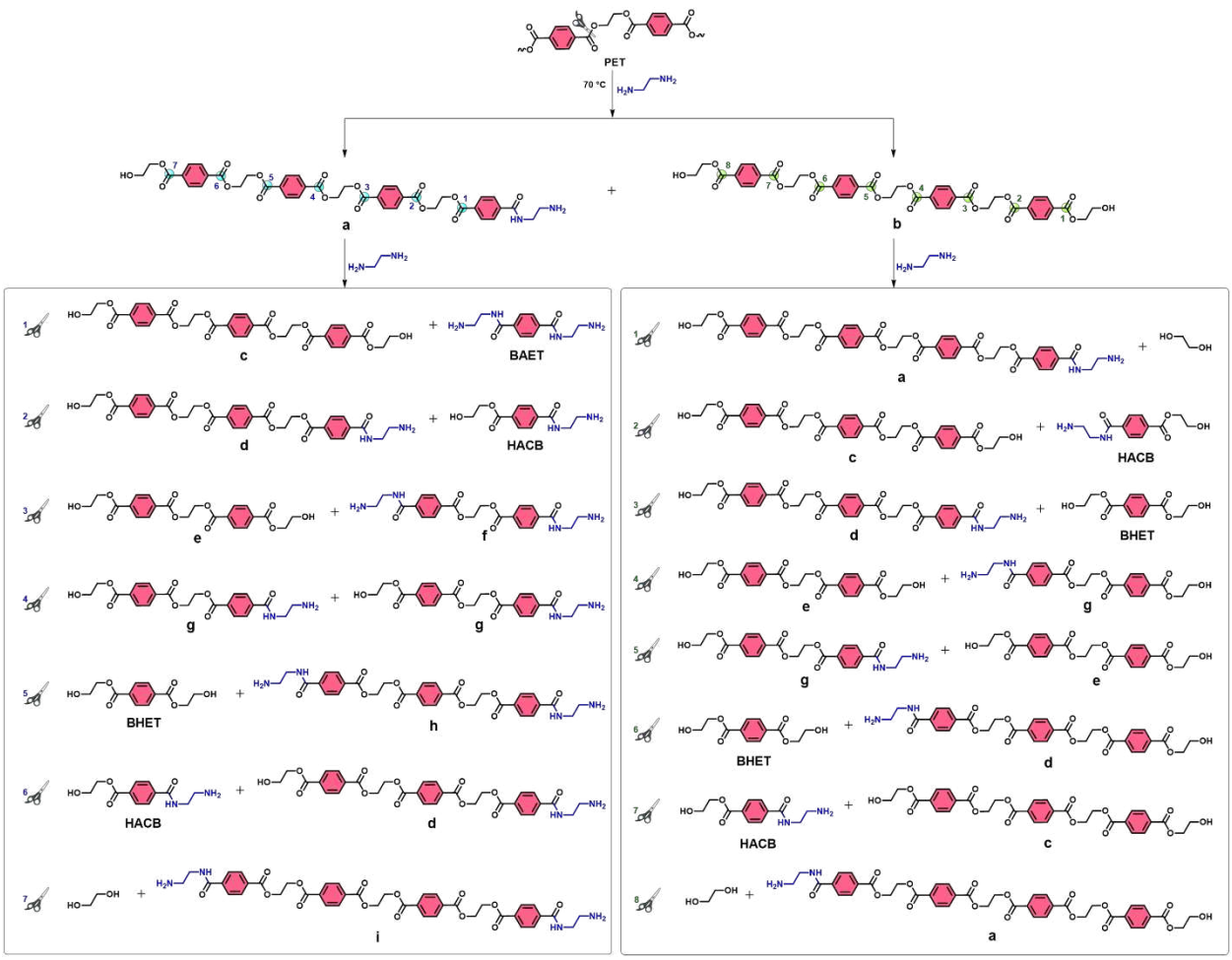
3.8 Qualitative analysis of PET aminolysis products via HR-MS and SEM analyses

For the first time, we report the formation of various intermediates and oligomers (up to tetramers, $n = 4$) in the aminolysis reaction over the reaction duration of 1-7 h (**Scheme 3**), confirmed by HR-MS analysis (**Figure S14-S30, Supporting Information**). Complementary SEM images of PET and its depolymerized products over the same reaction period further illustrate the progressive

surface changes (**Figure 9**) during the reaction. In PET aminolysis, degradation typically begins at the polymer surface, particularly in amorphous regions where chains are less ordered and more accessible to chemical attack [81]. Accordingly, the pristine PET surface appears smooth and intact (**Figure 9a**), while the depolymerization initiates at the solid–liquid interface as EDA molecules diffuse into the polymer matrix, causing swelling and enabling nucleophilic attack of $–NH_2$ groups on activated carbonyls of PET. The activation of carbonyl groups is facilitated by α-Al_2O_3 550, which enhances electrophilicity and accelerates the nucleophilic attack of the -NH_2 group of EDA. As the reaction progresses, after 1 h surface cracks on PET was observed (**Figure 9b**), increasing the exposed area and leading to the formation of two major tetrameric intermediates: an amide-based tetramer (**a in Scheme 3, and Figure S18, Supporting Information**) containing seven carbonyl sites (C=O, **labeled 1–7**) and an ester-based tetramer (**b in Scheme 3, and**, **Figure S19, Supporting Information**) containing eight sites (C=O, **labeled 1–8**): each serving as a potential site for EDA attack, giving rise to distinct products. After 2 h, slight roughening of the surface was observed (**Figure 9c**), while at 3 h, the surface became irregular, with pits and holes (**Figure 9d**), indicating structural weakening as EDA penetrated deeper. At this stage, cleavage at the 1st C=O of amide-based tetramer (**a in Scheme 3, and Figure S18, Supporting Information**) generates trimeric ester-based oligomer (**c in Scheme 3, and Figure S20, Supporting Information**) and BAET (**Figure S8, Supporting Information**), whereas cleavage at the 2nd C=O yields trimeric amide-based oligomer (**d in Scheme 3, and Figure S21, Supporting Information**) and 2-hydroxyethyl 4-((2-aminoethyl) carbamoyl) benzoate (**HACB in Scheme 3, and Figure S15, Supporting Information**). With continued depolymerization, at 4-5 h, visible cracks appear (**Figure 9e, f**) [81], and cleavage at the 3rd C=O produces a dimeric ester-based oligomer (**e in Scheme 3, and Figure S22, Supporting Information**) and a dimeric diamide-based oligomer (**f in Scheme 3, and Figure S23, Supporting Information**). Further diffusion of EDA into the polymer matrix promotes deeper bond scission, and cleavage at the 4th C=O yields a dimeric amide-based oligomer (**g in Scheme 3, and Figure S24, Supporting Information**). Severe surface erosion is evident later at 6-7 h (**Figure 9g, h**), consistent with catalyst-driven degradation, and cleavage at 5th C=O produces bis(2-hydroxyethyl) terephthalate (**BHET in Scheme 3, and Figure S14, Supporting Information**) together with a trimeric diamide-based oligomer (**h in Scheme 3, and Figure S25, Supporting Information**). Notably, the 6th C=O follows a similar pathway to the 2nd C=O, while cleavage at the 7th C=O gives a tetrameric diamide-based oligomer (**i in Scheme 3, and Figure S26, Supporting Information**) with ethylene glycol (**Figure S12, Supporting Information**) as a byproduct.

A parallel mechanism operates in the ester-based tetramer (**b in Scheme 3, and Figure S19, Supporting Information**). Due to its symmetry, cleavages at positions 1–8, 2–7, 3–6, and 4–5 generate equivalent products. Specifically, cleavage at 1st C=O regenerates amide-based tetramer (**a in Scheme 3, and Figure S18, Supporting Information**) with ethylene glycol (**Figure S12, Supporting Information**), while cleavage at 2nd C=O affords trimeric ester-based oligomer (**c in Scheme 3, and Figure S20, Supporting Information**) and HACB (**Scheme 3, and Figure S15, Supporting Information**). Cleavage at 3rd C=O produces trimeric amide-based oligomer (**d**

in Scheme 3, and Figure S21, Supporting Information) and BHET (**Scheme 3, and Figure S14, Supporting Information**), whereas cleavage at 4th C=O gives dimeric ester-based oligomer (**e in Scheme 3, and Figure S22, Supporting Information**) and dimeric amide-based oligomer (**g in Scheme 3, and Figure S24, Supporting Information**). The formation of BAET (**Figure S8, Supporting Information**), the AOET dimer (**Figure S9, Supporting Information**), the BAET trimer (**Figure S16, Supporting Information**), and the BAET tetramer (**Figure S17, Supporting Information**) follows the same process shown in **Scheme 2**. Overall, SEM analysis demonstrates that PET degradation proceeds via a surface-driven catalytic pathway, strongly dependent on reaction time.



Scheme 3: α-Al_2O_3 550-directed bond scission pathways in PET aminolysis, forming various intermediates and oligomers.

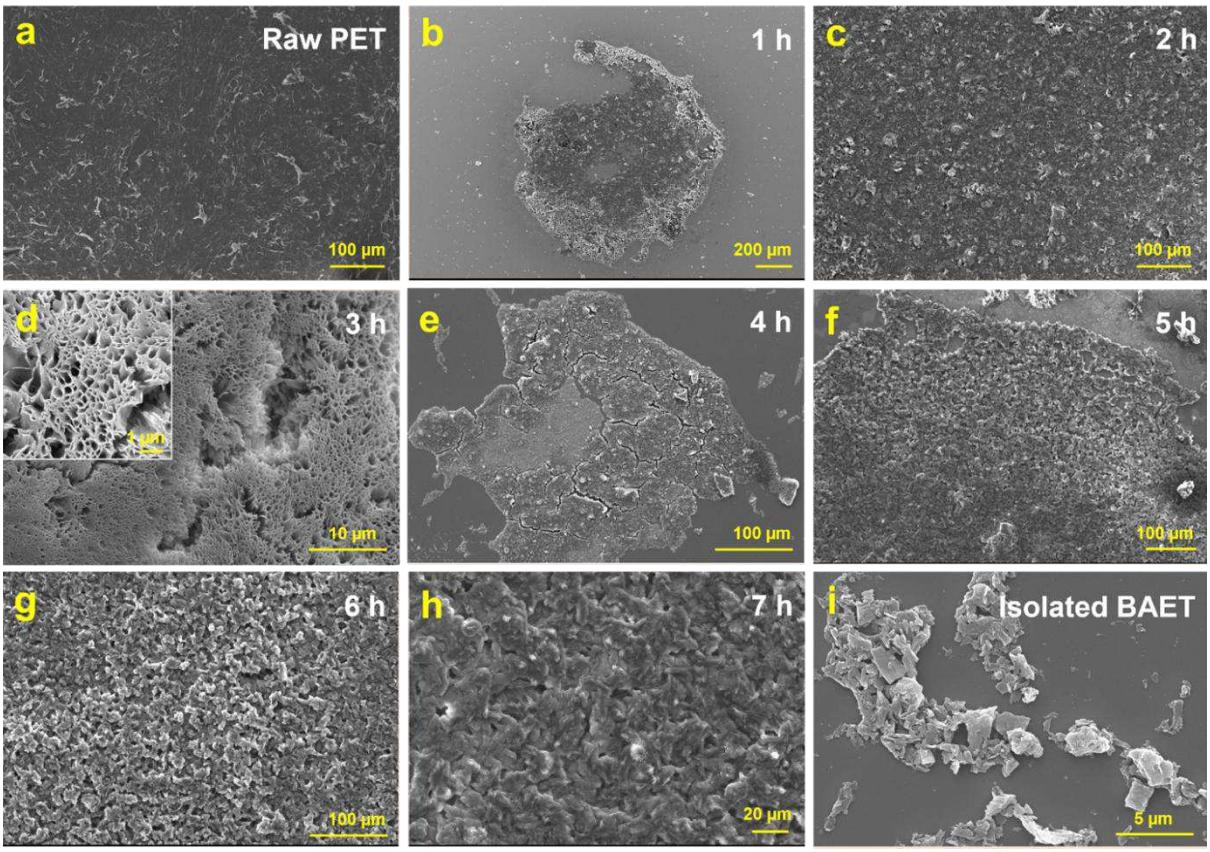
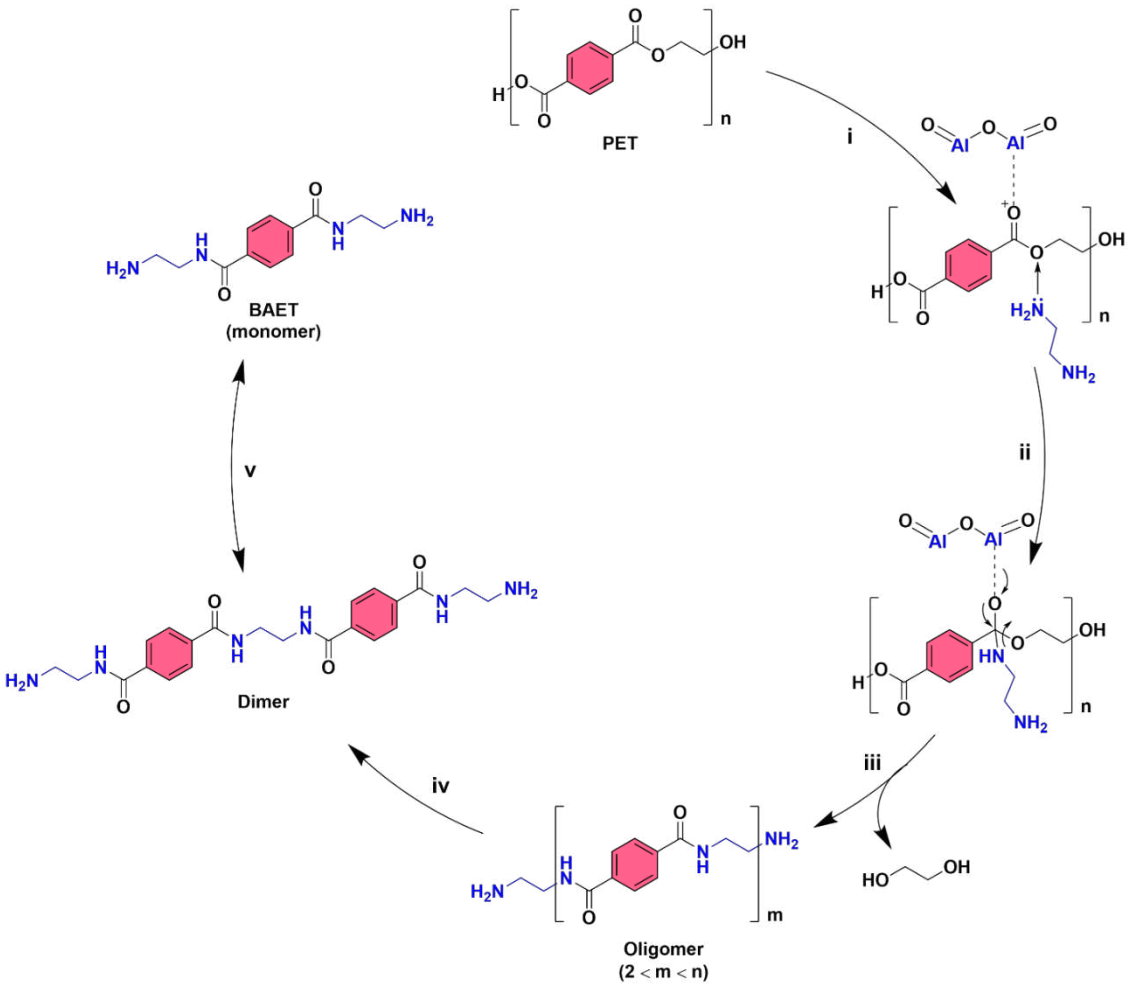


Figure 9. SEM images of (a) neat PET fakes, (b-h) reaction mixture of residual PET after reacting with ethylene diamine for the duration of 1 h, 2 h, 3 h, 4 h, 5 h, 6 h, and 7 h, and (i) isolated BAET (reaction temperature = 70 °C and molar ratio of PET:ED = 1:15).

3.9 Probable reaction mechanism for PET aminolysis

PET aminolysis proceeds through a transesterification pathway, where acid sites on the catalyst facilitate a nucleophilic attack[20,27]. The α-Al_2O_3 550 catalyst showed the best efficiency in the aminolysis of PET with EDA (92% yield of BAET, **entry 2**, **Table 2).** The NH_3-TPD analysis confirms that the α-Al_2O_3 550 catalyst has stronger acid sites, along with the weak acid sites, whereas the α-Al_2O_3 500 and α-Al_2O_3 600 catalysts exhibit the weak acid sites only (**Figure 7d**). As confirmed by SEM analysis, the presence of hierarchical pores in the α-Al_2O_3 550 catalyst, with well-defined grain boundaries throughout the sample, which can provide abundant active sites (**Figure 5a,b**), is another vital factor in achieving the optimum yield of BAET. These hierarchical pores on the surface, edges, and corners (**Figure 5c,d**), which could be the low-coordinated electron-deficient active sites, and surface area (56 m^2/g, **entry 2**, **Table 1**) of the α-Al_2O_3 550 catalyst, are advantageous for the reaction, as they can improve the adsorption and diffusion of the reactant molecules during the aminolysis reaction.

Based on these findings, **Scheme 4** illustrates a possible reaction mechanism for the aminolysis of PET with EDA over inexpensive α-Al_2O_3 550 to yield BAET. In this pathway, activation of PET carbonyl groups is essential, and α-Al_2O_3 550 facilitates this process owing to its abundant acid sites (**Figure 7d**). Once activated, the electrophilic carbonyl groups in PET ester bonds become susceptible to nucleophilic attack by the –NH_2 groups of EDA (**step i, Scheme 4**). As a result, the rearrangements of bonds in **step ii, Scheme 4,** lead to the release of ethylene glycol (**Figure S12**, **Supporting Information**) as a byproduct (**step iii, Scheme 4**). The PET undergoes aminolytic cleavage, where EDA reacts with the ester linkages to generate intermediate oligomers ($2 < n < m$). The formation of various oligomers (**Section 3.8)** during the reaction was confirmed by the HR-MS (**Figures S16-30, Supporting Information**). The incorporation of amine groups in oligomers is confirmed by FT-IR analysis (**Figure S3, Supporting Information**), giving a N–H stretching band corresponding to secondary (3281 cm^{-1}) amines. Besides, the reactions proceed (**Scheme 2**) via the interaction of EDA with the oligomer fragments to get AOET (dimer, **Figure S6, S9**, **Supporting Information**) (**step iv, Scheme 4**). This reaction proceeds in a controlled, stepwise manner, ultimately yielding BAET (**Figure S4, S8**, **Supporting Information**) as the final monomeric product, and this step is reversible as we have optimized the reaction conditions (**Figure 8 and step v, Scheme 4)**.



Scheme 4: Possible mechanism of PET aminolysis to the BAET monomer over the α-Al_2O_3 550 catalyst.

4. Conclusions

A novel α-Al_2O_3 catalyst with unique characteristics of hierarchical porous structure, nanosheet-like morphology, surface-engineered grain boundaries, and optimum amount of acid sites was developed for PET upcycling reaction using ethylenediamine as both the reagent and solvent. Under optimized reaction conditions, the α-Al_2O_3 550 catalyst showed complete polymer conversion, with 92% isolated yield of BAET. The sustainability and versatile catalytic efficiency of α-Al_2O_3 550 were further validated through gram-scale reactions (5 g) and its successful application to various colored PET materials (white, green, and blue). The α-Al_2O_3 550 catalyst is stable structurally and morphologically, as confirmed by powder XRD, XPS, and TEM analyses. This process is environmentally sustainable, as confirmed by the green chemistry metrics.

Supporting Information. Characterization details of powder XRD, Raman, SEM, TEM, AFM, N_2 adsorption-desorption, XPS, NMR, HR-MS, FT-IR, AFM, TGA, and DSC. HR-TEM of fresh

α-Al_2O_3 550 catalysts, XPS analysis of fresh and spent α-Al_2O_3 550 catalysts, FT-IR of PET, AOET (dimer), and BAET. NMR and HR-MS of BAET and AOET (dimer). DSC and TGA of PET, BAET, and AOET (dimer). Aminolysis of various-colored PET bottles. Green chemistry metrics and carbon balance percentage calculations for PET aminolysis. HR-MS analysis of monomer and oligomers.

Data Availability Statement

The data set used and/or analyzed during the current study is available from the corresponding author upon reasonable request.

Conflicts of interest

The authors declare no conflicts of interest.

Acknowledgements

M.A.K. is thankful to IITH and MoE for providing a PhD fellowship. B.S. acknowledges MHRD and PMRF for the fellowship. P.S. and G.M. acknowledge the funding support from MoE-STARS (project ID: 2023-0038) and ANRF (project ID: CRG/2023/000197).

References

(1) Feng, S.; Nguyen, P. T. T.; Ma, X.; Yan, N. Photorefinery of Biomass and Plastics to Renewable Chemicals Using Heterogeneous Catalysts. *Angewandte Chemie International Edition* 2024, *63* (37). https://doi.org/10.1002/anie.202408504.

(2) Manal, A. K.; Shivhare, A.; Lande, S.; Srivastava, R. Synergistic Catalysis for Promoting Selective C–C/C–O Cleavage in Plastic Waste: Structure–Activity Relationship and Rational Design of Heterogeneous Catalysts for Liquid Hydrocarbon Production. *Chemical Communications* 2024, *60* (90), 13143–13168. https://doi.org/10.1039/D4CC03261F.

(3) Al-Naji, M.; Antonietti, M. Turning Polyethylene Waste to Hydrocarbons Using a Sustainable Acidic Carbocatalyst. *ChemSusChem* 2023, *16* (9). https://doi.org/10.1002/cssc.202201991.

(4) Van Vaerenbergh, T.; Vikanova, K.; Wu, X.; Van Waeyenberg, J.; Smeyers, B.; van Leuven, H.; Sels, B. Hydrogen Production from Plastics: A Comprehensive Review of Thermochemical Pathways, Process Optimization and Sustainability Insights. *J Environ Chem Eng* 2025, *13* (5), 117929. https://doi.org/10.1016/j.jece.2025.117929.

(5) Singhal, R.; Nayak, R. R.; Singh, S.; Yadav, R. K.; Singh, R. V.; Gupta, N. K. Ultraresponsive Donor–Acceptor System for Transforming Poly(Lactic) Acid into Amino

Acids with Visible Light. *ACS Applied Engineering Materials* 2025, *3* (1), 98–107. https://doi.org/10.1021/acsaenm.4c00597.

(6) Pottinger, A. S.; Geyer, R.; Biyani, N.; Martinez, C. C.; Nathan, N.; Morse, M. R.; Liu, C.; Hu, S.; de Bruyn, M.; Boettiger, C.; Baker, E.; McCauley, D. J. Pathways to Reduce Global Plastic Waste Mismanagement and Greenhouse Gas Emissions by 2050. *Science (1979)* 2024, *386* (6726), 1168–1173. https://doi.org/10.1126/science.adr3837.

(7) Singh, N.; Walker, T. R. Plastic Recycling: A Panacea or Environmental Pollution Problem. *npj Materials Sustainability* 2024, *2* (1), 17. https://doi.org/10.1038/s44296-024-00024-w.

(8) Anwar, M.; Konnova, M. E.; Dastgir, S. Circular Plastic Economy for Sustainable Development: Current Advances and Future Perspectives. *RSC Sustainability* 2025, *3* (9), 3724–3840. https://doi.org/10.1039/D5SU00225G.

(9) Ellis, L. D.; Rorrer, N. A.; Sullivan, K. P.; Otto, M.; McGeehan, J. E.; Román-Leshkov, Y.; Wierckx, N.; Beckham, G. T. Chemical and Biological Catalysis for Plastics Recycling and Upcycling. *Nat Catal* 2021, *4* (7), 539–556. https://doi.org/10.1038/s41929-021-00648-4.

(10) Guo, Z.; Lim, J. S. K.; Ng, K. W. J.; Yan, W.; Gupta, N.; Hu, X. M. Direct One-Step Controlled Partial Depolymerization and Upcycling of Poly(Ethylene Terephthalate) into Hyperbranched Oligomeric Ionogel. *ACS Sustain Chem Eng* 2023, *11* (4), 1394–1404. https://doi.org/10.1021/acssuschemeng.2c05911.

(11) Cupertino, G. F. M.; Silva, Á. M. da; Pereira, A. K. S.; Delatorre, F. M.; Ucella-Filho, J. G. M.; Souza, E. C. de; Profeti, D.; Profeti, L. P. R.; Oliveira, M. P.; Saloni, D.; Luque, R.; Dias Júnior, A. F. Co-Pyrolysis of Biomass and Polyethylene Terephthalate (PET) as an Alternative for Energy Production from Waste Valorization. *Fuel* 2024, *362*, 130761. https://doi.org/10.1016/j.fuel.2023.130761.

(12) Sajwan, D.; Sharma, A.; Sharma, M.; Krishnan, V. Upcycling of Plastic Waste Using Photo-, Electro-, and Photoelectrocatalytic Approaches: A Way toward Circular Economy. *ACS Catal* 2024, *14* (7), 4865–4926. https://doi.org/10.1021/acscatal.4c00290.

(13) Cheng, J.; Xie, J.; Xi, Y.; Wu, X.; Zhang, R.; Mao, Z.; Yang, H.; Li, Z.; Li, C. Selective Upcycling of Polyethylene Terephthalate towards High-valued Oxygenated Chemical Methyl P-Methyl Benzoate Using a Cu/ZrO 2 Catalyst. *Angewandte Chemie International Edition* 2024, *63* (11). https://doi.org/10.1002/anie.202319896.

(14) Helmer, R.; Borkar, S. S.; Li, A.; Mahnaz, F.; Vito, J.; Bishop, M.; Iftakher, A.; Hasan, M. M. F.; Rangarajan, S.; Shetty, M. Tandem Methanolysis and Catalytic Transfer Hydrogenolysis of Polyethylene Terephthalate to P-Xylene Over Cu/ZnZrO x Catalysts.

Angewandte Chemie International Edition 2025, *64* (4). https://doi.org/10.1002/anie.202416384.

(15) Gao, Z.; Ma, B.; Chen, S.; Tian, J.; Zhao, C. Converting Waste PET Plastics into Automobile Fuels and Antifreeze Components. *Nat Commun* 2022, *13* (1), 3343. https://doi.org/10.1038/s41467-022-31078-w.

(16) Malik, N.; Li, J.; Agarwal, A.; Kratish, Y.; Marks, T. J. Thermodynamically Leveraged Solventless Aerobic Deconstruction of Polyethylene-Terephthalate Plastics over a Single-Site Molybdenum-Dioxo Catalyst. *Green Chemistry* 2025, *27* (9), 2427–2438. https://doi.org/10.1039/D4GC05916F.

(17) Wu, P.; Lu, G.; Cai, C. Cobalt–Molybdenum Synergistic Catalysis for the Hydrogenolysis of Terephthalate-Based Polyesters. *Green Chemistry* 2021, *23* (21), 8666–8672. https://doi.org/10.1039/D1GC02929K.

(18) Zhang, S.; Hu, Q.; Zhang, Y.-X.; Guo, H.; Wu, Y.; Sun, M.; Zhu, X.; Zhang, J.; Gong, S.; Liu, P.; Niu, Z. Depolymerization of Polyesters by a Binuclear Catalyst for Plastic Recycling. *Nat Sustain* 2023, *6* (8), 965–973. https://doi.org/10.1038/s41893-023-01118-4.

(19) Swapna, B.; Barnabas, M. B.; Moni Gogoi, P.; Bharali, P.; Madras, G.; Sudarsanam, P. Morphology-Tuned MnO *x* /TiO 2 Nanocatalysts for Recycling PET Plastic Waste Using Biomass-Derived Ethylene Glycol. *Nanoscale* 2025, *17* (17), 10620–10631. https://doi.org/10.1039/D4NR05373G.

(20) Swapna, B.; Singh, N.; Patowary, S.; Bharali, P.; Madras, G.; Sudarsanam, P. Efficient Glycolysis of Used PET Bottles into a High-Quality Valuable Monomer Using a Shape-Engineered MnO *x* Nanocatalyst. *Catal Sci Technol* 2024, *14* (19), 5574–5587. https://doi.org/10.1039/D4CY00823E.

(21) Fehér, Z.; Kiss, J.; Kisszékelyi, P.; Molnár, J.; Huszthy, P.; Kárpáti, L.; Kupai, J. Optimisation of PET Glycolysis by Applying Recyclable Heterogeneous Organocatalysts. *Green Chemistry* 2022, *24* (21), 8447–8459. https://doi.org/10.1039/D2GC02860C.

(22) Swapna, B.; Putla, S. B.; Ramesh, A.; Subrahmanyam, C.; Madras, G.; Sudarsanam, P. Catalytic Recycling of PET Waste Bottles into a Value-Added Amide Monomer Using a Heterogeneous Niobium Pentoxide Nanocatalyst. *Sustain Energy Fuels* 2024, *8* (22), 5170–5180. https://doi.org/10.1039/D4SE01136H.

(23) Hengameh Honarkar; Arjmand, F.; Askari, F.; Barikani, M. Structural Study on Aminolyzed Polyethylene Terephthalate. *Polymer Science, Series B* 2022, *64* (6), 800–809. https://doi.org/10.1134/S1560090422700646.

(24) Gao, L.; Shi, Y.; Li, Z.; Liu, Z.; Zhang, M.; Xu, Y.; Zou, X.; Yuan, X.; Hu, Y.; Guo, K. Endogenous Base Phosphine/Dimethyl Carbonate Catalyzed Depolymerization of Poly(Ethylene Terephthalate). *Catal Today* 2025, *450*, 115203. https://doi.org/10.1016/j.cattod.2025.115203.

(25) Swapna, B.; Fiba, C.; Barnabas, M. B.; Suryanarayana, R.; Sudarsanam, P. Catalytic Imidazolysis of PET Plastic Waste Using Self-Assembled NbO *x* Nanorods. *Chemical Communications* 2025, *61* (49), 8847–8850. https://doi.org/10.1039/D5CC01819F.

(26) Fukushima, K.; Lecuyer, J. M.; Wei, D. S.; Horn, H. W.; Jones, G. O.; Al-Megren, H. A.; Alabdulrahman, A. M.; Alsewailem, F. D.; McNeil, M. A.; Rice, J. E.; Hedrick, J. L. Advanced Chemical Recycling of Poly(Ethylene Terephthalate) through Organocatalytic Aminolysis. *Polym. Chem.* 2013, *4* (5), 1610–1616. https://doi.org/10.1039/C2PY20793A.

(27) Peterson, R.-J. L.; Neppel, E. P.; Peereboom, L.; Trinh, P. A.; Ofoli, R. Y.; Dorgan, J. R. Upcycling Waste PET: I. Ammonolysis Kinetics of Model Dimethyl Terephthalate and the Catalytic Effects of Ethylene Glycol. *ACS Sustain Chem Eng* 2025, *13* (10), 4120–4131. https://doi.org/10.1021/acssuschemeng.4c10238.

(28) George, N.; Kurian, T. Sodium Carbonate Catalyzed Aminolytic Degradation of PET. *Progress in Rubber, Plastics and Recycling Technology* 2016, *32* (3), 153–168. https://doi.org/10.1177/147776061603200304.

(29) Chen, Y.-H.; Ranganathan, P.; Lee, Y.-H.; Rwei, S.-P. New Strategy and Polymer Design to Synthesize Polyamide 66 (PA66) Copolymers with Aromatic Moieties from Recycled PET (RPET). *ACS Sustain Chem Eng* 2021, *9* (9), 3518–3528. https://doi.org/10.1021/acssuschemeng.0c08242.

(30) Pelckmans, M.; Renders, T.; Van de Vyver, S.; Sels, B. F. Bio-Based Amines through Sustainable Heterogeneous Catalysis. *Green Chemistry* 2017, *19* (22), 5303–5331. https://doi.org/10.1039/C7GC02299A.

(31) Liu, S. Q.; Venkataraman, S.; Ong, Z. Y.; Chan, J. M. W.; Yang, C.; Hedrick, J. L.; Yang, Y. Y. Overcoming Multidrug Resistance in Microbials Using Nanostructures Self-Assembled from Cationic Bent-Core Oligomers. *Small* 2014, *10* (20), 4130–4135. https://doi.org/10.1002/smll.201303921.

(32) Zhang, P.; Chen, X.; Bu, F.; Chen, C.; Huang, L.; Xie, Z.; Li, G.; Wang, X. Dual Coordination between Stereochemistry and Cations Endows Polyethylene Terephthalate Fabrics with Diversiform Antimicrobial Abilities for Attack and Defense. *ACS Appl Mater Interfaces* 2023, *15* (7), 9926–9939. https://doi.org/10.1021/acsami.2c19323.

(33) Fukushima, K.; Liu, S.; Wu, H.; Engler, A. C.; Coady, D. J.; Maune, H.; Pitera, J.; Nelson, A.; Wiradharma, N.; Venkataraman, S.; Huang, Y.; Fan, W.; Ying, J. Y.; Yang, Y. Y.; Hedrick, J. L. Supramolecular High-Aspect Ratio Assemblies with Strong Antifungal Activity. *Nat Commun* 2013, *4* (1), 2861. https://doi.org/10.1038/ncomms3861.

(34) Kuhn, M.; Wenzel, F. A.; Greve, C.; Kreger, K.; Schwartzkopf, M.; Schmidt, H.; Grüninger, H.; Herzig, E. M. Tailored Supramolecular Additives to Control the Crystallization Process and Morphology of MAPbI 3. *Small* 2025, *21* (9). https://doi.org/10.1002/smll.202410230.

(35) Xu, J.; Das, S.; Pathak, A. D.; Patra, A.; Shetty, S.; Hohl, D.; Car, R. Dynamic Metal–Support Interaction Dictates Cu Nanoparticle Sintering on Al 2 O 3 Surfaces. *ACS Nano* 2025, *19* (32), 29242–29254. https://doi.org/10.1021/acsnano.5c04622.

(36) Luo, W.; Liu, K.; Luo, T.; Fu, J.; Zhang, H.; Ma, C.; Chan, T.-S.; Kao, C.-W.; Lin, Z.; Chai, L.; Coote, M. L.; Liu, M. Promoting C–F Bond Activation for Perfluorinated Compounds Decomposition via Atomically Synergistic Lewis and Brønsted Acid Sites. *J Am Chem Soc* 2025, *147* (9), 7391–7399. https://doi.org/10.1021/jacs.4c15280.

(37) Deng, B.; Advincula, P. A.; Luong, D. X.; Zhou, J.; Zhang, B.; Wang, Z.; McHugh, E. A.; Chen, J.; Carter, R. A.; Kittrell, C.; Lou, J.; Zhao, Y.; Yakobson, B. I.; Zhao, Y.; Tour, J. M. High-Surface-Area Corundum Nanoparticles by Resistive Hotspot-Induced Phase Transformation. *Nat Commun* 2022, *13* (1), 5027. https://doi.org/10.1038/s41467-022-32622-4.

(38) Ji, Q.; Zhang, L.; Jiao, X.; Chen, D. Alpha Al 2 O 3 Nanosheet-Based Biphasic Aerogels with High-Temperature Resistance up to 1600 °C. *ACS Appl Mater Interfaces* 2023, *15* (5), 6848–6858. https://doi.org/10.1021/acsami.2c20272.

(39) Li, X.; Li, W.; Zhang, J.; Yin, W.; Xia, Y.; Xie, K. Porous Single-crystalline Centimeter-sized A-Al 2 O 3 Monoliths for Selective and Durable Non-oxidative Dehydrogenation of Ethane. *Angewandte Chemie International Edition* 2024, *63* (4). https://doi.org/10.1002/anie.202315274.

(40) Darabi, M.; Sharifi, E. M.; Vafaei, R.; Eshaghi, A.; Loghman-Estarki, M. R. The Effect of Amorphous Si3N4 Nanoparticles and Magnetized Distilled Water on the Mechanical Properties and Infrared Transmittance of α-Al2O3. *Sci Rep* 2025, *15* (1), 25504. https://doi.org/10.1038/s41598-025-11241-1.

(41) Song, Z.-H.; Muhammad, I.; Ren, T.-Z.; Abulizi, A.; Okitsu, K.; Li, H.-R.; Zhang, X.-J. Preparation of Al 2 O 3 Nanoparticles via Fluidized Roasting and Their Application in the Pyrolysis of Spent Mulching Film for Hydrocarbon Production. *ACS Sustainable Resource Management* 2025, *2* (3), 435–445. https://doi.org/10.1021/acssusresmgt.4c00436.

(42) Zhao, S.; Jin, Q.; Shi, Y.; Zhao, M.; Xu, H.; Shen, X.; Han, X.; Hong, X. Optimization of Short-Range Order in Amorphous AlO *x* Nanosheets for Enhanced Methane Oxidation. *Nano Lett* 2025, *25* (20), 8211–8219. https://doi.org/10.1021/acs.nanolett.5c01251.

(43) Zhu, L.; Lei, T.; Liu, X.; Yang, X.; Zhang, B.; Jiao, H.; Guo, W.; Teng, B.; Wen, X. Proton Transfers at the Water/Solid Interface of α-Al 2 O 3 –Supported Ni Clusters under Steam Reforming Conditions: An AIMD Study. *ACS Catal* 2024, *14* (16), 12342–12350. https://doi.org/10.1021/acscatal.4c02514.

(44) Jang, S.; Gun Oh, D.; Kim, H.; Hyun Kim, K.; Khivantsev, K.; Kovarik, L.; Hun Kwak, J. Controlling the Phase Transformation of Alumina for Enhanced Stability and Catalytic Properties. *Angewandte Chemie International Edition* 2024, *63* (15). https://doi.org/10.1002/anie.202400270.

(45) Jiang, W.; Cao, J.-P.; Huan, Z.-X.; Hu, X.; Tang, W.; Chen, C.-X.; Wang, H.-Y.; He, Z.-M.; Zhao, X.-Y.; Bai, H.-C. Relatively Electron-Rich Ni Nanoparticles Supported on α-Al 2 O 3 for High-Efficiency Hydrogenolysis of Lignin and Its Derivatives under Mild Conditions. *ACS Sustain Chem Eng* 2023, *11* (50), 17646–17661. https://doi.org/10.1021/acssuschemeng.3c04713.

(46) Pu, T.; Setiawan, A.; Foucher, A. C.; Guo, M.; Jehng, J.-M.; Zhu, M.; Ford, M. E.; Stach, E. A.; Rangarajan, S.; Wachs, I. E. Revealing the Nature of Active Oxygen Species and Reaction Mechanism of Ethylene Epoxidation by Supported Ag/α-Al 2 O 3 Catalysts. *ACS Catal* 2024, *14* (1), 406–417. https://doi.org/10.1021/acscatal.3c04361.

(47) Ma, X.; Luo, S.; Hua, Y.; Seetharaman, S.; Zhu, X.; Hou, J.; Zhang, L.; Wang, W.; Sun, Y. An Alumina Phase Induced Composite Transition Shuttle to Stabilize Carbon Capture Cycles. *Nat Commun* 2024, *15* (1), 7556. https://doi.org/10.1038/s41467-024-52016-y.

(48) Baldovino-Medrano, V. G.; Farin, B.; Gaigneaux, E. M. Establishing the Role of Graphite as a Shaping Agent of Vanadium–Aluminum Mixed (Hydr)Oxides and Their Physicochemical Properties and Catalytic Functionalities. *ACS Catal* 2012, *2* (3), 322–336. https://doi.org/10.1021/cs200465h.

(49) Ruan, H. D.; Frost, R. L.; Kloprogge, J. T. Comparison of Raman Spectra in Characterizing Gibbsite, Bayerite, Diaspore and Boehmite. *Journal of Raman Spectroscopy* 2001, *32* (9), 745–750. https://doi.org/10.1002/jrs.736.

(50) Rkiouak, L.; Tang, M. J.; Camp, J. C. J.; McGregor, J.; Watson, I. M.; Cox, R. A.; Kalberer, M.; Ward, A. D.; Pope, F. D. Optical Trapping and Raman Spectroscopy of Solid Particles. *Phys. Chem. Chem. Phys.* 2014, *16* (23), 11426–11434. https://doi.org/10.1039/C4CP00994K.

(51) Ashkin, M.; Parker, J. H.; Feldman, D. W. Temperature Dependence of the Raman Lines of α-Al2O3. *Solid State Commun* 1968, *6* (6), 343–346. https://doi.org/10.1016/0038-1098(68)90152-X.

(52) Musuvadhi Babulal, S.; Li, J.; Dabur, D.; Wu, H.-F. Fluorescent Nanoprobe Based on 2D Al 2 O 3 Nanosheets for Clioquinol Detection. *ACS Appl Nano Mater* 2025, *8* (10), 4958–4966. https://doi.org/10.1021/acsanm.4c05772.

(53) Varma, A.; Mukasyan, A. S.; Rogachev, A. S.; Manukyan, K. V. Solution Combustion Synthesis of Nanoscale Materials. *Chem Rev* 2016, *116* (23), 14493–14586. https://doi.org/10.1021/acs.chemrev.6b00279.

(54) Carlos, E.; Martins, R.; Fortunato, E.; Branquinho, R. Solution Combustion Synthesis: Towards a Sustainable Approach for Metal Oxides. *Chemistry – A European Journal* 2020, *26* (42), 9099–9125. https://doi.org/10.1002/chem.202000678.

(55) Siddique, F.; Gonzalez-Cortes, S.; Mirzaei, A.; Xiao, T.; Rafiq, M. A.; Zhang, X. Solution Combustion Synthesis: The Relevant Metrics for Producing Advanced and Nanostructured Photocatalysts. *Nanoscale* 2022, *14* (33), 11806–11868. https://doi.org/10.1039/D2NR02714C.

(56) Wen, W.; Wu, J.-M. Nanomaterials via Solution Combustion Synthesis: A Step Nearer to Controllability. *RSC Adv.* 2014, *4* (101), 58090–58100. https://doi.org/10.1039/C4RA10145F.

(57) Amrute, A. P.; Łodziana, Z.; Schreyer, H.; Weidenthaler, C.; Schüth, F. High-Surface-Area Corundum by Mechanochemically Induced Phase Transformation of Boehmite. *Science (1979)* 2019, *366* (6464), 485–489. https://doi.org/10.1126/science.aaw9377.

(58) Hütner, J. I.; Conti, A.; Kugler, D.; Mittendorfer, F.; Kresse, G.; Schmid, M.; Diebold, U.; Balajka, J. Stoichiometric Reconstruction of the Al 2 O 3 (0001) Surface. *Science (1979)* 2024, *385* (6714), 1241–1244. https://doi.org/10.1126/science.adq4744.

(59) Bai, J.; Tang, C.; Zhao, S.; Liu, S.; Wang, W.; Han, C.; Zhao, Q.; Shen, Y. Few-Layer Molybdenite-Derived MoS2 Nanosheets and SnO2 Nanostructures Heterojunctions for High-Performance NH3 Detection: Insights from Experimental and DFT Analysis. *Chemical Engineering Journal* 2025, *509*, 161374. https://doi.org/10.1016/j.cej.2025.161374.

(60) McHale, J. M.; Auroux, A.; Perrotta, A. J.; Navrotsky, A. Surface Energies and Thermodynamic Phase Stability in Nanocrystalline Aluminas. *Science (1979)* 1997, *277* (5327), 788–791. https://doi.org/10.1126/science.277.5327.788.

(61) Murata, K.; Shiotani, T.; Ohyama, J.; Wakabayashi, R.; Maruoka, H.; Kimura, T.; Satsuma, A. Relationship between Penta-Coordinated Al 3+ Sites in the Al 2 O 3 Supports and CH 4 Combustion Activity of Pd/Al 2 O 3 Catalysts. *Catal Sci Technol* 2021, *11* (7), 2374–2378. https://doi.org/10.1039/D1CY00098E.

(62) Roostaiy Ghalehnooiy, M.; Golhosseini, R.; Mohammadrezaei, A. Trimetallic Catalyst, Prepared by Ultrasonic -Impregnation Method for Selective Hydrogenation of Acetylene: Investigation of Potassium Addition to Fe-Pd/α-Al2O3 Catalyst. *Reaction Kinetics, Mechanisms and Catalysis* 2023, *136* (4), 2003–2020. https://doi.org/10.1007/s11144-023-02449-1.

(63) Song, X.; Yang, C.; Li, X.; Wang, Z.; Pei, C.; Zhao, Z.-J.; Gong, J. On the Role of Hydroxyl Groups on Cu/Al 2 O 3 in CO 2 Hydrogenation. *ACS Catal* 2022, *12* (22), 14162–14172. https://doi.org/10.1021/acscatal.2c03591.

(64) Ravi, K.; Kachgunde, H.; Dasireddy, V. D. B. C.; Mensah, J.; Lee, A. F.; Biradar, A. V.; Wilson, K. Bifunctional Rh/Al-SBA-15 Catalysed Cascade Hydroformylation and Hydroxyalkylation of Alkenes to Fuel Precursors. *Catal Sci Technol* 2025, *15* (10), 3149–3156. https://doi.org/10.1039/D5CY00171D.

(65) Fitzgerald, J. J.; Piedra, G.; Dec, S. F.; Seger, M.; Maciel, G. E. Dehydration Studies of a High-Surface-Area Alumina (Pseudo-Boehmite) Using Solid-State 1 H and 27 Al NMR. *J Am Chem Soc* 1997, *119* (33), 7832–7842. https://doi.org/10.1021/ja970788u.

(66) Wilson, S. J. The Dehydration of Boehmite, γ-AlOOH, to γ-Al2O3. *J Solid State Chem* 1979, *30* (2), 247–255. https://doi.org/10.1016/0022-4596(79)90106-3.

(67) Arun Kumar, M.; Swapna, B.; Kalbande, P. N.; Yalagandula, L.; Singh, S. A.; Sudarsanam, P. Selective Synthesis of Renewable Diesel Fuel Precursors via C–C Condensation of Biomass-Derived Furans Using a Niobium Oxide Nanocatalyst. *ACS Sustain Chem Eng* 2024, *12* (43), 15923–15934. https://doi.org/10.1021/acssuschemeng.4c03886.

(68) Subha, P.; Luo, Q.; Li, H.; Sudarsanam, P. One-Pot, *in Situ* Reductive Catalytic Approach for Biomass Furfural-Based Secondary Amines under Ambient Conditions. *Green Chemistry* 2025. https://doi.org/10.1039/D5GC02500A.

(69) Ashwani, C. A.; Subha, P.; Yalagandula, L.; Len, C.; Singh, S. A.; Sudarsanam, P. Synergistic Nanoalloy PdCu/TiO 2 Catalyst for *in Situ* Hydrogenation of Biomass-Derived Furfural at Room Temperature. *Green Chemistry* 2025, *27* (26), 7820–7832. https://doi.org/10.1039/D5GC00006H.

(70) Wang, F.; Ma, J.; He, G.; Chen, M.; Zhang, C.; He, H. Nanosize Effect of Al 2 O 3 in Ag/Al 2 O 3 Catalyst for the Selective Catalytic Oxidation of Ammonia. *ACS Catal* 2018, *8* (4), 2670–2682. https://doi.org/10.1021/acscatal.7b03799.

(71) Rimaz, S.; Chen, L.; Monzón, A.; Kawi, S.; Borgna, A. Enhanced Selectivity and Stability of Pt-Ge/Al2O3 Catalysts by Ca Promotion in Propane Dehydrogenation. *Chemical Engineering Journal* 2021, *405*, 126656. https://doi.org/10.1016/j.cej.2020.126656.

(72) Svintsitskiy, D. A.; Kibis, L. S.; Stadnichenko, A. I.; Slavinskaya, E. M.; Romanenko, A. V.; Fedorova, E. A.; Stonkus, O. A.; Doronkin, D. E.; Marchuk, V.; Zimina, A.; Casapu, M.; Grunwaldt, J.; Boronin, A. I. Insight into the Nature of Active Species of Pt/Al 2 O 3 Catalysts for Low Temperature NH 3 Oxidation. *ChemCatChem* 2020, *12* (3), 867–880. https://doi.org/10.1002/cctc.201901719.

(73) Wang, Y.; Xu, W.; Li, C.; Yang, Y.; Geng, Z.; Zhu, T. Effects of IrO2 Nanoparticle Sizes on Ir/Al2O3 Catalysts for the Selective Catalytic Oxidation of Ammonia. *Chemical Engineering Journal* 2022, *437*, 135398. https://doi.org/10.1016/j.cej.2022.135398.

(74) Yang, X.; Li, Q.; Lu, E.; Wang, Z.; Gong, X.; Yu, Z.; Guo, Y.; Wang, L.; Guo, Y.; Zhan, W.; Zhang, J.; Dai, S. Taming the Stability of Pd Active Phases through a Compartmentalizing Strategy toward Nanostructured Catalyst Supports. *Nat Commun* 2019, *10* (1), 1611. https://doi.org/10.1038/s41467-019-09662-4.

(75) Sharma, P.; Lochab, B.; Kumar, D.; Roy, P. K. Sustainable Bis-Benzoxazines from Cardanol and PET-Derived Terephthalamides. *ACS Sustain Chem Eng* 2016, *4* (3), 1085–1093. https://doi.org/10.1021/acssuschemeng.5b01153.

(76) Hoang, C. N.; Dang, Y. H. Aminolysis of Poly(Ethylene Terephthalate) Waste with Ethylenediamine and Characterization of α,ω-Diamine Products. *Polym Degrad Stab* 2013, *98* (3), 697–708. https://doi.org/10.1016/j.polymdegradstab.2012.12.026.

(77) Tsang, A. C. H.; Wong, M. Y. L.; Tsang, C.-W.; Suen, D. W.-S.; Lu, X.-Y. Development of AlN-Loaded PET Separators from Waste Water Bottle Plastics with Superior Thermal Characteristics for next-Generation Lithium-Ion Batteries. *RSC Adv* 2025, *15* (7), 5452–5461. https://doi.org/10.1039/D4RA06478J.

(78) Thomas, D.; Ranjan, R.; George, B. K. Co-Al-CO 3 Layered Double Hydroxide: An Efficient and Regenerable Catalyst for Glycolysis of Polyethylene Terephthalate. *RSC Sustainability* 2023, *1* (9), 2277–2286. https://doi.org/10.1039/D3SU00304C.

(79) Kasmi, N.; Bäckström, E.; Hakkarainen, M. Open-Loop Recycling of Post-Consumer PET to Closed-Loop Chemically Recyclable High-Performance Polyimines. *Resour Conserv Recycl* 2023, *193*, 106974. https://doi.org/10.1016/j.resconrec.2023.106974.

(80) Sharma, D.; Choudhary, P.; Kumar, S.; Krishnan, V. Integrated Chemical Upcycling of Poly(Ethylene Terephthalate) Waste to Multiple Value-Added Products Catalyzed by Ni 2 P Supported on SiO2 : From Trash-to-Treasure. *ACS ES&T Engineering* 2025. https://doi.org/10.1021/acsestengg.5c00357.

(81) Rong, C.; Yan, D.; Li, J.; Feng, J.; Xin, J.; Zhou, Q.; Li, Y.; Xu, J.; Lu, X. An Effective Strategy for Degrading Waste PET Plastic into Regenerated DMT with Nearly Equivalent Methanol at Relatively Low Temperature. *Chem Eng Sci* 2025, *315*, 121859. https://doi.org/10.1016/j.ces.2025.121859.

Supplementary Files

This is a list of supplementary files associated with this preprint. Click to download.

- SINPGAsiaMaterials.docx